



# Emerging hollow artificial photosynthetic system with S-scheme heterojunction sandwiched between layered redox cocatalysts for overall CO<sub>2</sub> reduction and H<sub>2</sub>O oxidation



Xingwei Zhang <sup>a,1</sup>, Yili Song <sup>b,1</sup>, Xiangyue Niu <sup>c</sup>, Xinyuan Lin <sup>c</sup>, Shuxian Zhong <sup>a</sup>, Hongjun Lin <sup>a</sup>, Botao Teng <sup>b,\*</sup>, Song Bai <sup>a,c,\*\*</sup>

<sup>a</sup> College of Geography and Environmental Sciences, Zhejiang Normal University, Jinhua, Zhejiang 321004, PR China

<sup>b</sup> Tianjin Key Laboratory of Brine Chemical Engineering and Resource Eco-utilization, College of Chemical Engineering and Materials Science, Tianjin University of Science and Technology, Tianjin 300457, PR China

<sup>c</sup> Key Laboratory of the Ministry of Education for Advanced Catalysis Materials, College of Chemistry and Materials Science, Zhejiang Normal University, Jinhua, Zhejiang 321004, PR China

## ARTICLE INFO

### Keywords:

S-scheme heterojunction  
Earth-abundant layered cocatalysts  
Hollow sandwiched structure  
CO<sub>2</sub> reduction  
H<sub>2</sub>O oxidation

## ABSTRACT

The development of artificial photosynthesis is challenged by nonstoichiometric photocatalytic reaction of CO<sub>2</sub> with H<sub>2</sub>O. Herein, a delicate hollow multi-shelled nanoreactor with S-scheme heterojunction sandwiched between layered noble-metal-free redox cocatalysts is fabricated, which exhibits excellent photocatalytic performance for overall CO<sub>2</sub>-to-CO reduction and H<sub>2</sub>O-to-O<sub>2</sub> oxidation with stoichiometric ratio of the evolved reduction and oxidation products. The synergy of the sandwiched heterojunction and spatially separated dual cocatalysts on the inner/outer sides: (i) promotes the separation and transfer of powerful photoexcited charges towards opposite directions; (ii) maneuvers the occurrence of surface redox reactions in different spaces through lowering the thermodynamic barriers, and (iii) hinders the occurrence of side reactions and photocorrosion on the semiconductor surface. Consequently, the charge separation, transfer and consumption are well balanced, and the photocatalytic activity, selectivity and stability are perfectly optimized. It is expected that this novel design can be extended to other semiconductor heterojunctions towards high-efficient photoredox catalysis.

## 1. Introduction

Mimicking natural photosynthesis to convert CO<sub>2</sub> with H<sub>2</sub>O into value-added chemicals or fuels via solar energy holds promise to close the carbon cycle and fulfill the energy demand [1–4]. Unfortunately, its practical application is restricted by low solar-to-chemical energy conversion efficiency because of insufficient light utilization, rapid electron-hole recombination, sluggish catalytic reactivity, and undesirable side/reverse reactions in most of established semiconductor photocatalysts [5,6]. Particularly, it is difficult for a single-component semiconductor photocatalyst to simultaneously possess wide optical absorption range and strong redox capabilities. Besides, some photocatalysts only work in the presence of a hole scavenger resulted from mismatched energy band structure [7,8], while others exhibit

incompatible O<sub>2</sub> evolution much lower than stoichiometric ratio owing to unbalanced transfer and consumption of photogenerated electrons and holes [9,10]. Generally, the mobility of holes is significantly lower than that of electrons [11]. Meanwhile, four-electron-proton coupled oxygen evolution reaction is a slow kinetics process requiring relatively high energy to overcome the barrier, thus becoming the bottleneck of overall redox reactions [12]. Therefore, it is highly desirable to develop elaborated artificial photosynthetic systems not only allowing highly active and selective photoreduction of CO<sub>2</sub> to target product, but also enabling perfect cooperation of CO<sub>2</sub> reduction and H<sub>2</sub>O oxidation.

Step-scheme (S-scheme) heterojunction, a rising star in photocatalysis, has demonstrated its multiple advantages to achieve overall redox reactions, which not only settles the trade-off between light absorption and redox potentials of mono-component semiconductor, but

\* Corresponding author.

\*\* Corresponding author at: College of Geography and Environmental Sciences, Zhejiang Normal University, Jinhua, Zhejiang 321004, PR China.

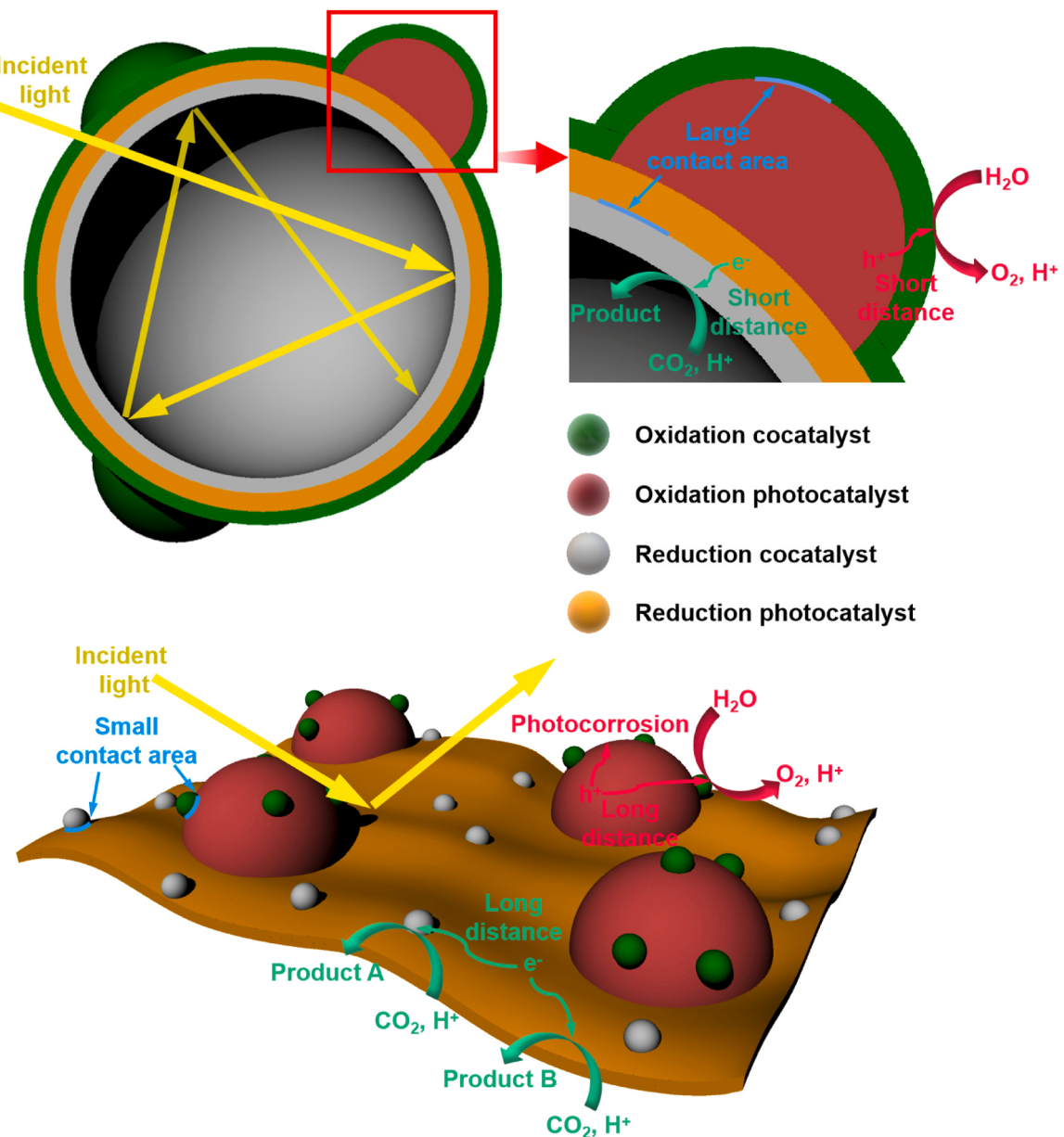
E-mail addresses: [tbt@zjnu.cn](mailto:tbt@zjnu.cn) (B. Teng), [songbai@zjnu.edu.cn](mailto:songbai@zjnu.edu.cn) (S. Bai).

<sup>1</sup> These authors contributed equally to this work.

also balances the separation and transfer of photocarriers [13,14]. A typical S-scheme heterojunction is comprised of a reduction photocatalyst (RP) and an oxidation photocatalyst (OP) with narrow band gap ( $E_g$ ) and staggered band alignment. With the photoexcitation of RP and OP, weak OP electrons transmit cross the interface and recombine with RP holes, thus separating powerful RP electrons and OP holes for redox reactions. Enabled by the S-scheme heterojunction design, there have been considerable photoactivity enhancements in  $\text{CO}_2$  reduction and other applications [15–17]. Nevertheless, existing S-scheme heterojunctions still suffer from unsatisfactory  $\text{CO}_2$  conversion efficiencies, poor product selectivities, and mismatched  $\text{O}_2$  evolution, since the lack of robust and well-defined redox sites on the semiconductor surface modulating the reaction kinetics, regulating the  $\text{CO}_2$  reduction pathways, and balancing the electron-hole consumption [18].

Introduction of proper cocatalysts represents an effective strategy to overcome above obstacles and optimize the catalytic reactivities of S-scheme heterojunctions [19–21]. Reduction and oxidation cocatalysts respectively trap photoelectrons and holes from light-harvesting

semiconductors and provide highly active sites for redox reactions. However, a simple implantation of dual cocatalysts with a random distribution only gives rise to more serious carrier recombination and severe back reactions [22,23]. It is of utmost importance to anchor reduction and oxidation cocatalysts separately on the RP and OP surface of an S-scheme heterojunction [24]. Selective photodeposition of noble metal (e.g. Pt, Pd and Au) and their derivatives (e.g.  $\text{IrO}_2$  and  $\text{RuO}_2$ ) may be a potential method, which however is unsustainable and economically unsound due to scarcity and high cost of precious metal [25,26]. Furthermore, the vast majority of reported cocatalysts are discrete on the semiconductor surface. As illustrated in **Scheme 1**, the small contact area between light-harvesting semiconductor and cocatalyst cannot provide sufficient channel for interfacial charge transfer, and the long carrier-migration distance from the former to the latter inevitably increases the probability of charge recombination loss. Resulted from the sluggish charge transfer, part of active charges move to cocatalyst while others retain on the exposed semiconductor surface for redox reactions. The diverse active sites of cocatalyst and semiconductor cause different



**Scheme 1.** Schematic illustrating the advantages of sandwiching S-scheme heterojunction between layered redox cocatalysts to construct a hollow artificial photosynthetic system over decorating S-scheme heterojunction with discrete redox cocatalysts.

reaction paths, lowering the product selectivity [27]. Meanwhile, the unconsumed carriers on the semiconductor surface may also induce photocorrosion, attenuating the stability of photocatalyst [28,29]. Therefore, constructing novel artificial photosynthetic systems for better coupling of S-scheme heterojunction and noble-metal-free redox cocatalysts is crucial to take full utilization of their advantages and realize overall conversion of  $\text{CO}_2$  with  $\text{H}_2\text{O}$  in high activity, selectivity and stability.

Recently, two-dimensional (2D) layered materials, such as carbonenes (graphene, graphdiyne) [30,31], phosphorenes (black phosphorus) [32], MXene ( $\text{Ti}_3\text{C}_2\text{T}_x$ ) [33], transition metal dichalcogenides ( $\text{MoS}_2$ ,  $\text{WS}_2$ ) and hydroxides ( $\text{Ni(OH)}_2$ ,  $\text{Co(OH)}_2$ ) [34–37] have emerged as effective noble-metal-free redox cocatalysts in photocatalysis. Different from particulate cocatalysts, as depicted in **Scheme 1**, 2D structure of cocatalysts allow their face-to-face contact with semiconductors, broadening the space for interfacial charge transfer and shortening the distance for carrier travelling from the latter to the former. Furthermore, the coating of layered cocatalysts can prevent encapsulated semiconductors from participating in side reactions and protect them from photocorrosion. On the other sides, hollow semiconductor nanostructure has shown intrinsic merits in photocatalysis: (i) reinforces the photon absorption via multiple light reflection and scattering in the inner cavities; (ii) provides an ideal platform for the spatial separation of redox cocatalysts inside/outside of the nano-/microreactors [38,39]. Bearing the above points in mind, herein, a hollow artificial photosynthetic system with S-scheme heterojunction ( $\text{ZnIn}_2\text{S}_4/\text{Fe}_2\text{O}_3$ ) sandwiched between layered reduction (carbon) and oxidation ( $\text{Ni(OH)}_2$ ) cocatalysts has been constructed for significantly enhanced photocatalytic performance in overall  $\text{CO}_2$  reduction coupled with  $\text{H}_2\text{O}$  oxidation. In the as-synthesized  $\text{C@ZnIn}_2\text{S}_4/\text{Fe}_2\text{O}_3@\text{Ni(OH)}_2$  photoreactor (labeled as CZFN), the hollow carbon supporter and  $\text{Ni(OH)}_2$  outer layer: (i) drive the flow of electrons and holes with higher redox capacities in opposite directions, maximizing the charge separation efficiency and balancing the consumption of them; (ii) separate the reduction and oxidation half reactions inside and outside the reactor, restraining the occurrence of backward reaction; (iii) improve the adsorption and activation of reactants, lowering the rate-limiting barriers for  $\text{CO}_2$ -to-CO and  $\text{H}_2\text{O}$ -to- $\text{O}_2$  transformation. As a result, the artificial system exhibits superb activity and selectivity in CO evolution with an apparent quantum efficiency (AQE) of 1.98% at 420 nm. Additionally, the yields of reduction and oxidation products meet almost stoichiometric ratio. To the best of our knowledge, such a hollow photosynthetic system design with Janus layered dual cocatalysts on the two sides of an S-scheme heterojunction has rarely been reported before.

## 2. Experimental section

### 2.1. Synthesis of $\text{C@ZnIn}_2\text{S}_4$ and $\text{ZnIn}_2\text{S}_4$

In a typical synthesis, 3 mL of glycerol and 20 mL of  $\text{H}_2\text{O}$  were injected into a 50 mL round bottom flask, the pH of the solution was adjusted to 2.5 by HCl (0.5 M), which was ultrasonicated for 3 min to obtain a uniform solution. Subsequently,  $\text{ZnCl}_2$  (27.2 mg, 0.2 mmol),  $\text{InCl}_3 \cdot 4 \text{H}_2\text{O}$  (58.6 mg, 0.2 mmol) and thioacetamide (30 mg, 0.4 mmol) were added to the above suspension and stirred for 30 min, which is followed by the addition of hollow carbon spheres (2 mg). The resulting mixture was stirred for 10 min and then heated at 80 °C for 2 h. After naturally cooling down to room temperature, the product was collected by centrifuging, washed with ethanol and water thoroughly, and dried at 45 °C in a vacuum. Pristine  $\text{ZnIn}_2\text{S}_4$  nanosheets were prepared under the same experimental conditions as  $\text{C@ZnIn}_2\text{S}_4$  except the absence of hollow carbon spheres.

### 2.2. Synthesis of $\text{Fe}_2\text{O}_3$ and $\text{C@ZnIn}_2\text{S}_4/\text{Fe}_2\text{O}_3$

In a typical synthesis of  $\text{Fe}_2\text{O}_3$  nanocubes,  $\text{Fe}(\text{NO}_3)_3 \bullet 9 \text{H}_2\text{O}$

(64.5 mg, 0.16 mmol) was dissolved in 40 mL of dimethylformamide to form a clear solution after stirring for 5 min at room temperature. The solution was then transferred into a 50 mL Teflon-lined stainless steel autoclave, which was then heated at 180 °C for 6 h. After cooling down to room temperature, the resultant product is washed three times with water and ethanol to remove possible remaining cations and anions, and dried at 45 °C in a vacuum. As for the synthesis of  $\text{C@ZnIn}_2\text{S}_4/\text{Fe}_2\text{O}_3$ ,  $\text{C@ZnIn}_2\text{S}_4$  and  $\text{Fe}_2\text{O}_3$  were re-dispersed in water to form 5 and 3 mg  $\text{mL}^{-1}$  aqueous suspension, respectively. Subsequently, 1 mL of  $\text{Fe}_2\text{O}_3$  suspension was dropwise added into 1 mL of  $\text{C@ZnIn}_2\text{S}_4$  suspension, which is followed by the ultrasonic treatment of the mixed suspension for 5 min. The resultant product was separated by centrifugation, washed with water three times, and dried at 45 °C in a vacuum.

### 2.3. Synthesis of CZFN and $\text{Ni(OH)}_2$

$\text{Ni}(\text{NO}_3)_2 \cdot 6 \text{H}_2\text{O}$  (72.8 mg, 0.25 mmol) and 50 mL of  $\text{H}_2\text{O}$  were injected into a 100 mL round bottom flask. Subsequently,  $\text{C}_6\text{H}_5\text{O}_7\text{Na}_3$  (6.5 mg, 0.025 mmol), hexamethylenetetramine (35 mg, 0.25 mmol), and 40 mg of  $\text{C@ZnIn}_2\text{S}_4/\text{Fe}_2\text{O}_3$  were added to above suspension and stirred for 30 min. The resulting mixture was stirred for 10 min and then heated at 90 °C for 10 h. After naturally cooling down to room temperature, the product was collected by centrifuging, washed with ethanol and water thoroughly, and dried at 45 °C in a vacuum. Pristine  $\text{Ni(OH)}_2$  nanosheets were prepared under the same experimental conditions as CZFN except the absence of  $\text{C@ZnIn}_2\text{S}_4/\text{Fe}_2\text{O}_3$  precursor.

### 2.4. Synthesis of binary, ternary, and quaternary counterparts

$\text{C/Fe}_2\text{O}_3$  and  $\text{ZnIn}_2\text{S}_4/\text{Fe}_2\text{O}_3$  were synthesized under the equivalent reaction conditions as  $\text{C@ZnIn}_2\text{S}_4/\text{Fe}_2\text{O}_3$  except the use of pure hollow carbon,  $\text{ZnIn}_2\text{S}_4$  instead of  $\text{C@ZnIn}_2\text{S}_4$  as a precursor, respectively.  $\text{ZnIn}_2\text{S}_4@\text{Ni(OH)}_2$ ,  $\text{Fe}_2\text{O}_3@\text{Ni(OH)}_2$ ,  $\text{C@ZnIn}_2\text{S}_4@\text{Ni(OH)}_2$ ,  $\text{C/Fe}_2\text{O}_3@\text{Ni(OH)}_2$ , and  $\text{ZnIn}_2\text{S}_4/\text{Fe}_2\text{O}_3@\text{Ni(OH)}_2$  were prepared by following the same procedure as CZFN except the use of  $\text{ZnIn}_2\text{S}_4$ ,  $\text{Fe}_2\text{O}_3$ ,  $\text{C@ZnIn}_2\text{S}_4$ ,  $\text{C/Fe}_2\text{O}_3$ , and  $\text{ZnIn}_2\text{S}_4/\text{Fe}_2\text{O}_3$  instead of  $\text{C@ZnIn}_2\text{S}_4/\text{Fe}_2\text{O}_3$  as a precursor.  $\text{C/Fe}_2\text{O}_3@\text{ZnIn}_2\text{S}_4$  was synthesized under the same experimental conditions as  $\text{C@ZnIn}_2\text{S}_4$  except the use of  $\text{C/Fe}_2\text{O}_3$  instead of hollow carbon spheres as a precursor. As for the synthesis of  $\text{C/Fe}_2\text{O}_3 @\text{ZnIn}_2\text{S}_4@\text{Ni(OH)}_2$ ,  $\text{C/Fe}_2\text{O}_3@\text{ZnIn}_2\text{S}_4$  was first prepared according to the synthetic procedure of  $\text{C@ZnIn}_2\text{S}_4$  except the use of  $\text{C/Fe}_2\text{O}_3$  instead of hollow carbon spheres as a precursor, which is followed by the coating of  $\text{Ni(OH)}_2$  outer layer according to the synthetic procedure of CZFN except the use of  $\text{C/Fe}_2\text{O}_3@\text{ZnIn}_2\text{S}_4$  instead of  $\text{C@ZnIn}_2\text{S}_4/\text{Fe}_2\text{O}_3$  as a precursor.

### 2.5. Photocatalytic $\text{CO}_2$ reduction measurements

To investigate the photocatalytic performance of the samples in  $\text{CO}_2$  reduction, 20 mg of photocatalyst was dispersed in 2 mL water, and was dispersed on a flat glass plate at the bottom of a 150 mL photocatalytic reactor (Beijing Perfectlight, China). Prior to the test, the reactor loaded with the catalyst was first purged with high purity  $\text{CO}_2$  for 15 min in the dark. Then the light-irradiation experiment was performed by using a 300 W Xe lamp (PLS-SXE300D/300DUV, Beijing Perfectlight, China) with visible light as the illumination source, which was realized using both a 420-nm cutoff filter (long-wave-pass) and a 780-nm cutoff filter (short-wave-pass). The power density of visible light ( $420 < \lambda < 780 \text{ nm}$ ) was measured to be  $100 \text{ mW cm}^{-2}$  using a radiometer (FZ-A, China). The photocatalytic reaction was conducted for 4 h under stirring at a rate of 500 rpm. The gaseous mixture was analyzed using a gas chromatograph (GC-2014, Shimadzu) with Ar as the carrier gas. The amounts of  $\text{H}_2$  and  $\text{O}_2$  were determined using a thermal conductivity detector (TCD). CO was converted to  $\text{CH}_4$  by using a methanation reactor and then analyzed using the flame ionization detector (FID). During the stability test, the photocatalyst was collected after each run

and then reused for the photocatalytic reaction. Isotope-labeling experiments were performed using  $^{13}\text{CO}_2$  instead of  $^{12}\text{CO}_2$ , and the products were analyzed using gas chromatography-mass spectrometry (7890B/5977 A, Agilent). The product selectivity was calculated according to the average evolution rates of the reduction products as well as the electrons required to generate products using the following equation:

$$\text{CO selectivity} = 2 v(\text{CO})/[2 v(\text{CO}) + 2 v(\text{H}_2)] \times 100\% \quad (1)$$

## 2.6. Apparent quantum efficiency (AQE) measurements

AQE was measured in an identical photosynthesis process except the 420 nm monochromatic incident light provided by a light-emitting diodes (LEDs). AQE is defined as the ratio of the photocatalytic electron consumption ( $N_{\text{electron}}$ ) to the photons flux per hour ( $N_{\text{photon}}$ ), which is calculated according to the formula:

$$\text{AQE}(\%) = N_{\text{electron}}/N_{\text{photon}} = 2 N(\text{CO})/[(I \times A \times t)/(E_{\text{photon}} \times N_A)] \quad (2)$$

where  $N(\text{CO})$  represents the amount of CO;  $I$  is the incident light intensity;  $A$  is the illumination area which is controlled to  $0.82 \text{ cm}^2$ ;  $t$  is the illumination time;  $N_A$  is Avogadro's constant; and  $E_{\text{photon}}$  is the average single photon energy, which is figured out using the equation:

$$E_{\text{photon}} = hc/\lambda \quad (3)$$

where  $h$  is the Planck constant,  $c$  is the speed of light, and  $\lambda$  is the wavelength.

## 2.7. Electrochemical and photoelectrochemical measurements

5.0 mg of as-prepared samples was uniformly mixed with 30  $\mu\text{L}$  of ethanol, which were then uniformly coated onto a  $1 \text{ cm} \times 1 \text{ cm}$  indium tin oxide (ITO) glass. Subsequently, the coated ITO glass was dried at  $50^\circ\text{C}$  for 6 h in vacuum. The electrochemical and photoelectrochemical measurements were performed on a CHI 760E electrochemical station (Shanghai Chenhua, China). A standard three electrode system was used consisting of the ITO glass as work electrode, an Ag/AgCl electrode as reference electrode, and a Pt foil as counter electrode, which were inserted in a quartz cell containing 0.5 M  $\text{Na}_2\text{SO}_4$  solution electrolyte. The electrochemical impedance spectroscopy (EIS) was performed in the  $10^{-1}$  to  $10^5 \text{ Hz}$  frequency range with an AC voltage amplitude of 10 mV at an applied potential of 0.1 V vs. Ag/AgCl. Photoelectrochemical tests were performed in ambient conditions under irradiation of a 300 W Xe lamp (PLS-SXE300D/300DUV, Beijing Perfectlight, China). The power density of the visible light ( $420 < \lambda < 780 \text{ nm}$ ) was measured to be  $100 \text{ mW cm}^{-2}$ . The photocurrent density vs. time (I-t) curves of the prepared photoelectrodes was operated at an applied potential of 0.4 V vs. Ag/AgCl under chopped light irradiation (light on/off cycles: 30 s) for 600 s. Transient open-circuit voltage decay (OCVD) measurements were taken for a total of 800 s, and the visible light was switched on and off after 100 and 400 s from the start, respectively. The average lifetimes of the photogenerated carriers ( $\tau_n$ ) were then estimated from the open-circuit voltage ( $V_{\text{oc}}$ ) decay according to the following Equation:

$$\tau_n = -\frac{k_B T}{q} \left( \frac{dV_{\text{oc}}}{dt} \right)^{-1} \quad (4)$$

where  $\tau_n$  represents the average lifetime,  $V_{\text{oc}}$  is open-circuit voltage,  $k_B$  is the Boltzmann constant,  $T$  is the temperature (in Kelvin), and  $q$  is the unsigned charge of an electron. Linear sweep voltammetry (LSV) for electrochemical  $\text{CO}_2$  reduction was carried out in an Ar-saturated and  $\text{CO}_2$ -saturated 0.5 M  $\text{KHCO}_3$  solution ( $\text{pH} = 7.3$ ) with a scan rate of  $10 \text{ mV s}^{-1}$ , respectively. The working electrode was the glassy carbon electrode instead of ITO glass. For electrochemical  $\text{O}_2$  evolution

reaction, linear sweep voltammetry (LSV) was carried out in 0.5 M KOH solution (40 mL,  $\text{pH} = 13.69$ ) with a scan rate of  $10 \text{ mV s}^{-1}$ . The potentials against the Ag/AgCl reference electrode were converted to the RHE reference scale based on the following equation:

$$E(\text{vs-RHE}) = E(\text{vs-Ag/AgCl}) + 0.21 \text{ V} + 0.0591 \times \text{pH} \quad (5)$$

## 2.8. Sample characterizations

Transmission electron microscopy (TEM), high-resolution TEM (HRTEM), scanning TEM (STEM) and energy-dispersive spectroscopy (EDS) mapping profiles were taken on a JEOL JEM-2100 F field-emission high-resolution transmission electron microscope operated at 200 kV. Scanning electron microscopy (SEM) characterization was carried out on a Zeiss Gemini 300 scanning electron micro-analyzer with an accelerating voltage of 3 kV. Powder X-ray powder diffraction (XRD) patterns were collected on a D8 Advance X-ray diffractometer with Non-monochromated Cu-K $\alpha$  X-Ray. X-ray photoelectron spectroscopy (XPS) was collected on an ESCALab 250 X-ray photoelectron spectrometer, using nonmonochromatized Al-K $\alpha$  X-ray as the excitation source. In situ irradiated XPS measurements with external visible light source irradiation ( $420 < \lambda < 780 \text{ nm}$ , PLS-SXE300D/300DUV, Beijing Perfectlight, China) were performed on the basis of XPS measurements. Brunauer-Emmett-Teller (BET) specific surface areas and  $\text{N}_2$  adsorption were measured by using a Quantachrome autosorb iQ analyzer at 77 K.  $\text{CO}_2$  adsorption was tested using the Quantachrome autosorb iQ analyzer at 298 K. Stead-state photoluminescence (PL) emission spectra were examined using a photoluminescence spectrometer (FLS980, Edinburgh Instruments Ltd.) with a 370-nm excitation wavelength. Raman measurement was carried out on a Renishaw inVia Reflex Raman spectroscope under excitation wavelength of 532 nm. UV-vis diffuse reflectance data were recorded in the spectral region of 200–800 nm with a Cary-7000 series UV-vis-NIR spectrophotometer. Tauc plots were derived from the UV-vis diffuse reflectance spectra according to the equation:

$$(\alpha h\nu)^2 = A(h\nu - E_g) \quad (6)$$

where  $\alpha$ ,  $h\nu$  and  $E_g$  are the absorption coefficient, photon energy and optical bandgap, respectively. The signal of  $\bullet\text{O}_2^-$  and  $\bullet\text{OH}$  was examined by electron paramagnetic resonance (EPR) spectrometer (Bruker EPR EMXplus) at 9.843 GHz in darkness and under visible light irradiation, respectively. In situ diffuse reflectance Fourier transform infrared spectroscopy (DRIFTS) was conducted on a Nicolet iN10 Fourier transform infrared spectrometer. The  $\text{CO}_2/\text{H}_2\text{O}$  gas was introduced into the sample cell and maintained in darkness for 20 min, and then irradiated by visible light for 70 min

## 3. Results and discussion

### 3.1. Sample synthesis and characterization

The synthetic procedure of CZFN is illustrated in Fig. 1a, which starts with the preparation of hollow carbon nanospheres with  $\text{SiO}_2$  spheres as templates (step i and ii): monodispersed  $\text{SiO}_2$  spheres were firstly synthesized (Fig. S1a,b), followed by the modification and carbonization of polymer layer on the  $\text{SiO}_2$  surface (Fig. S1c,d), and finally the removal of the silica core to gain the hollow carbon (Fig. S1e,f) [40]. Scanning electron microscopy (SEM) image in Fig. 1b demonstrates the well-defined hollow carbon spheres with an average diameter of 403 nm, and the mesopore channels in the carbon shell can be seen clearly from TEM image (Fig. 1b and Fig. S2a). Afterwards,  $\text{ZnIn}_2\text{S}_4$  was in situ grown on the outer surface of carbon spheres to form a hollow  $\text{C}@\text{ZnIn}_2\text{S}_4$  core-shell structure (step iii). As revealed by SEM and TEM imaging, the exterior surface of carbon spheres is fully covered by

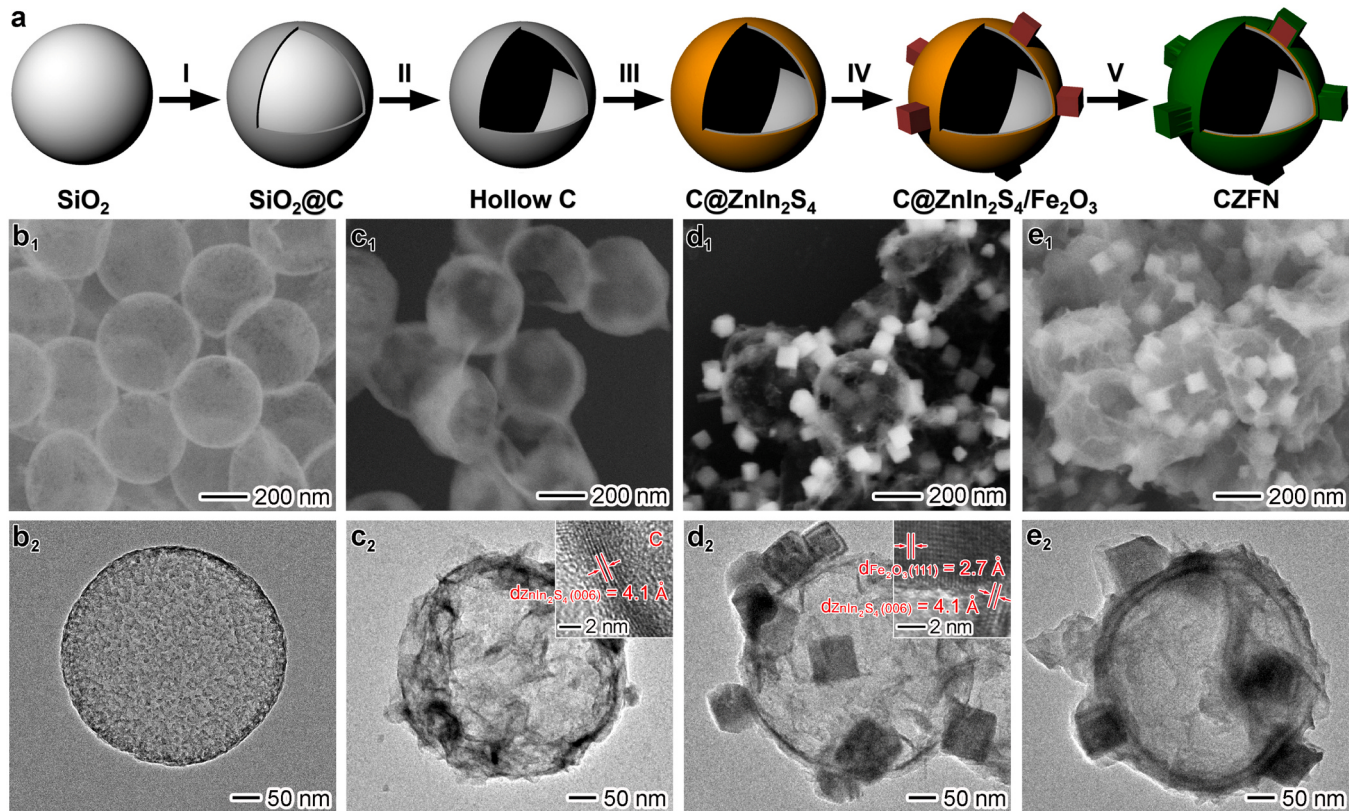


**Fig. 1.** Formation process of CZFN: (a) schematic illustrating the synthetic process of CZFN; (b-e) SEM and TEM images of (b) hollow C, (c) C@ZnIn<sub>2</sub>S<sub>4</sub>, (d) C@ZnIn<sub>2</sub>S<sub>4</sub>/Fe<sub>2</sub>O<sub>3</sub> and (e) CZFN.

wrinkled nanosheets with a lattice fringe spacing of 4.1 Å, corresponding to (006) crystal plane of hexagonal ZnIn<sub>2</sub>S<sub>4</sub> (Fig. 1c). In the next step, cubic Fe<sub>2</sub>O<sub>3</sub> nanocrystals were pre-synthesized (Fig. S3) [41] and deposited on the outer surface of C@ZnIn<sub>2</sub>S<sub>4</sub> to obtain C@ZnIn<sub>2</sub>S<sub>4</sub>/Fe<sub>2</sub>O<sub>3</sub> (step iv). SEM and TEM observation reveals that the single-crystalline Fe<sub>2</sub>O<sub>3</sub> nanocubes with an average edge length of 69.3 nm are uniformly anchored on the surface of ZnIn<sub>2</sub>S<sub>4</sub> supported by carbon spheres (Fig. 1d and Fig. S2b). Finally, the outer surface of C@ZnIn<sub>2</sub>S<sub>4</sub>/Fe<sub>2</sub>O<sub>3</sub> was coated with Ni(OH)<sub>2</sub> nanosheets to fabricate final CZFN (step v). The ultrathin Ni(OH)<sub>2</sub> layer coating on the surface of ZnIn<sub>2</sub>S<sub>4</sub> and Fe<sub>2</sub>O<sub>3</sub> can be clearly seen from SEM/TEM images in Fig. 1e. Besides, some Ni(OH)<sub>2</sub> nanosheets are also observed to bridge neighboring C@ZnIn<sub>2</sub>S<sub>4</sub>/Fe<sub>2</sub>O<sub>3</sub> to form interlaced networks (Fig. 2a,b). In view of the intimate contact between one face of Fe<sub>2</sub>O<sub>3</sub> nanocube with ZnIn<sub>2</sub>S<sub>4</sub>, Ni(OH)<sub>2</sub> outer layer only covers other five Fe<sub>2</sub>O<sub>3</sub> faces, forming a core-shell structure with Fe<sub>2</sub>O<sub>3</sub> core enclosed by ZnIn<sub>2</sub>S<sub>4</sub> interlayer and Ni(OH)<sub>2</sub> shell (Fig. 2c). In the selected area of the core-shell structure in Fig. 2c, HRTEM image shows clear lattice fringes with spacing of 2.7 and 2.1 Å, corresponding to (111) plane of  $\alpha$ -phase Fe<sub>2</sub>O<sub>3</sub> and (200) plane of cubic NiO, respectively (Fig. 2d). Since  $\alpha$ -Ni(OH)<sub>2</sub> can be easily transformed to NiO under electron beam irradiation, only HRTEM image of evolved NiO can be captured [42]. Further STEM image and the corresponding EDS mapping profiles visualize the elemental distribution of C, Zn, In, S, Fe, Ni and O in the CZFN, validating that the quaternary sample is composed of hollow carbon supporter, ZnIn<sub>2</sub>S<sub>4</sub> interlayer, Fe<sub>2</sub>O<sub>3</sub> core and Ni(OH)<sub>2</sub> outer shell (Fig. 2e). Apart from CZFN, bare ZnIn<sub>2</sub>S<sub>4</sub> and Ni(OH)<sub>2</sub> were also prepared by following the step iii and v synthetic process except the absence of hollow carbon and C@ZnIn<sub>2</sub>S<sub>4</sub>/Fe<sub>2</sub>O<sub>3</sub> precursor, respectively, both of which display flower-like hierarchical microspheres consisting of interweaving nanosheets (Fig. S4 and S5).

Spectroscopic characterizations of CZFN were performed by a combination of XRD, Raman spectroscopy, N<sub>2</sub> sorption isotherm, UV-vis diffuse reflectance spectroscopy and XPS with bare hollow C, ZnIn<sub>2</sub>S<sub>4</sub>,

Fe<sub>2</sub>O<sub>3</sub> and Ni(OH)<sub>2</sub> as reference samples. As depicted in Fig. 2f, all the diffraction peaks in the XRD patterns of ZnIn<sub>2</sub>S<sub>4</sub>, Fe<sub>2</sub>O<sub>3</sub> and Ni(OH)<sub>2</sub> match well with the standard card of hexagonal ZnIn<sub>2</sub>S<sub>4</sub> (JCPDS-65-2023), rhombohedral hematite (JCPDS-33-0664), and hexagonal Ni(OH)<sub>2</sub> (JCPDS-38-0715), respectively, while no distinct peak can be observed in the pattern of hollow C. The characteristic ZnIn<sub>2</sub>S<sub>4</sub>, Fe<sub>2</sub>O<sub>3</sub> and Ni(OH)<sub>2</sub> peaks can be simultaneously observed in the pattern of CZFN. Similar to XRD, Raman spectrum of CZFN exhibits typical peaks including well-documented D and G bands of hollow C, longitudinal optical modes (LO<sub>1</sub> and LO<sub>2</sub>) and transverse optical modes (TO<sub>2</sub>) of ZnIn<sub>2</sub>S<sub>4</sub>, A<sub>1g</sub> and E<sub>g</sub> modes of Fe<sub>2</sub>O<sub>3</sub>, and Ni-O stretching vibration of Ni(OH)<sub>2</sub> (Fig. 2g) [43-45]. According to N<sub>2</sub> adsorption-desorption measurement, BET surface area of hollow C, ZnIn<sub>2</sub>S<sub>4</sub>, Fe<sub>2</sub>O<sub>3</sub>, Ni(OH)<sub>2</sub> and CZFN is determined to be 380.1, 18.7, 4.2, 6.6 and 58.2 m<sup>2</sup> g<sup>-1</sup>, respectively, reflecting the critical function of hollow porous carbon in boosting the exposed area of CZFN for mass transport (Fig. 2h). Three possible reasons account for the obviously smaller BET surface area of CZFN relative to that of hollow C: (i) ZnIn<sub>2</sub>S<sub>4</sub> coverage, Fe<sub>2</sub>O<sub>3</sub> loading and Ni(OH)<sub>2</sub> coating, to some extent, block the pores of hollow C and prevent the mass transportation; (ii) a small amount of hollow C might have been damaged during the synthesis of CZFN; (iii) the mass contribution of ZnIn<sub>2</sub>S<sub>4</sub>, Fe<sub>2</sub>O<sub>3</sub> and Ni(OH)<sub>2</sub> gives rise to the decrease in the BET area of CZFN [46]. As revealed by UV-vis diffuse reflectance spectra in Fig. 2i, ZnIn<sub>2</sub>S<sub>4</sub>, Fe<sub>2</sub>O<sub>3</sub> and Ni(OH)<sub>2</sub> exhibit intrinsic bandgap absorption with absorption edge at ca. 470, 600 and 310 nm, respectively, while carbon spheres show broad optical absorption in UV-vis region but without a absorption edge, mainly owing to multiple light reflection and scattering inside the hollow chamber of the zero-bandgap material [47]. As for CZFN, the absorption spectrum is a simple superposition of those of the components involved.

The chemical states of the samples were investigated by XPS. Survey spectrum of CZFN mainly contains the peaks of C1s, Zn2p, In3d, S2p, Fe2p, Ni2p and O1s, in line with the elemental mapping analysis

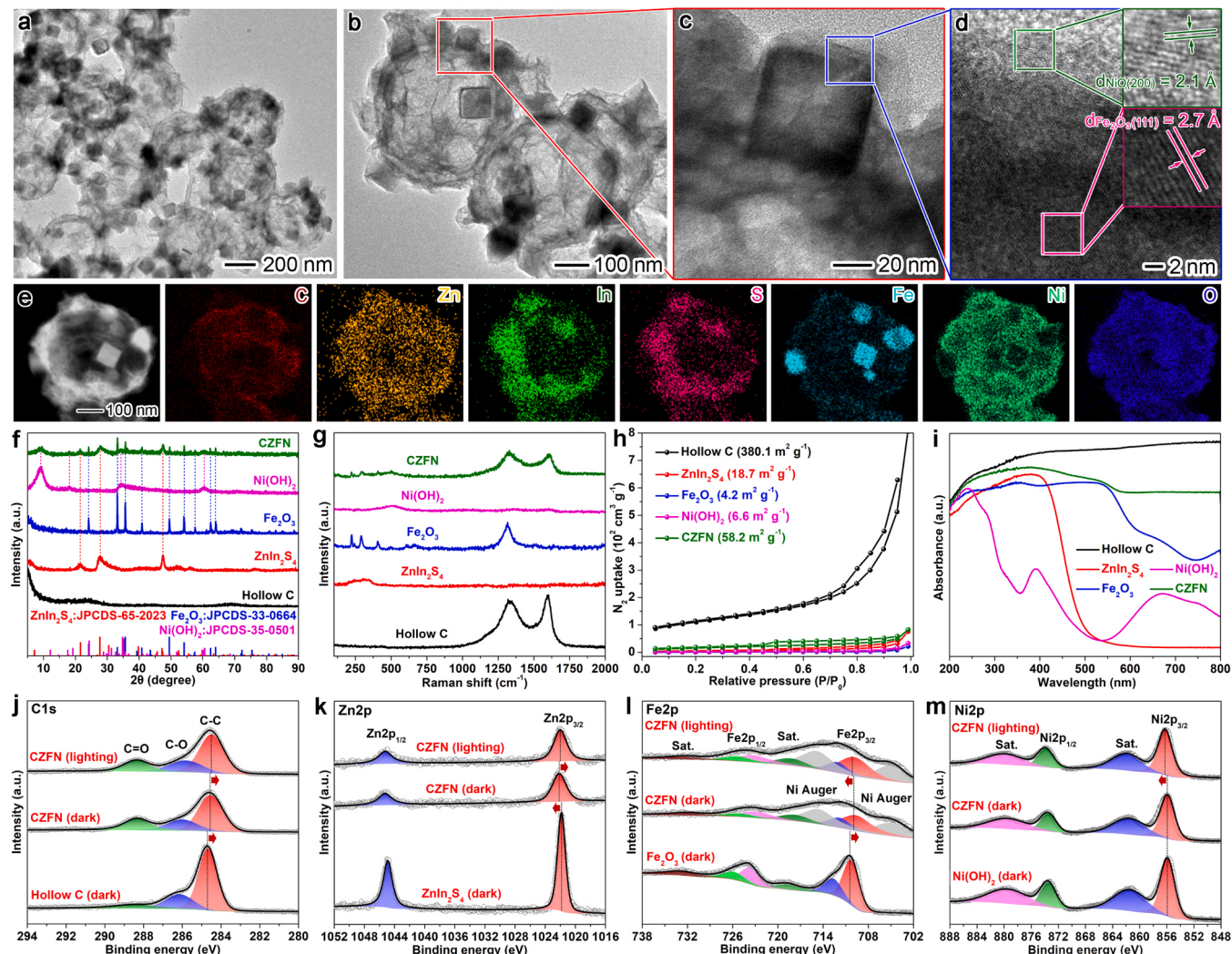


**Fig. 2.** Detailed characterizations of CZFN: (a-d) TEM and HRTEM images; (e) STEM image and corresponding EDS-mapping profiles; (f-m) spectroscopic characterizations of CZFN with hollow C,  $\text{ZnIn}_2\text{S}_4$ ,  $\text{Fe}_2\text{O}_3$  and  $\text{Ni(OH)}_2$  as reference samples: (f) XRD patterns, (g) Raman spectra, (h)  $\text{N}_2$  sorption isotherms, (i) UV-vis diffuse reflectance spectra, (j-m) high-resolution XPS spectra: (j) C1s, (k) Zn2p, (l) Fe2p and (m) Ni2p.

(Fig. S6a). The high-resolution C1s spectra can be deconvoluted to three peaks assigned to C-C, C-O and C=O of hollow C, respectively, and the corresponding binding energies shift to lower values when hollow C is comprised in the CZFN, inferring that carbon supporter acts as an electron-accumulating component (Fig. 2j). Similar phenomenon can be observed in the Zn2p spectrum, in which  $\text{Zn2p}_{3/2}$  and  $\text{Zn2p}_{1/2}$  binding energies of CZFN positively shift by 0.32 eV when compared with those of pristine  $\text{ZnIn}_2\text{S}_4$ , disclosing that  $\text{ZnIn}_2\text{S}_4$  becomes electron deficient upon the formation of the hybrid (Fig. 2k). The electron-deficient  $\text{ZnIn}_2\text{S}_4$  in the CZFN is further confirmed by the positive shifts of  $\text{In3d}_{3/2}/\text{In3d}_{5/2}$  and  $\text{S2p}_{1/2}/\text{S2p}_{3/2}$  peaks in the In3d and S2p spectra (Fig. S6b,c). The Fe2p spectra can be fitted to six peaks corresponding to  $\text{Fe2p}_{1/2}/\text{Fe2p}_{3/2}$  and satellite signals of  $\text{Fe}_2\text{O}_3$ , which move to lower binding energies and overlap with Ni Auger peaks in the case of CZFN, inferring the electron-withdrawing  $\text{Fe}_2\text{O}_3$  during the formation of the hybrid (Fig. 2l). Conversely, in the Ni2p spectra, no obvious shift occurs on  $\text{Ni2p}_{1/2}/\text{Ni2p}_{3/2}$  and satellite peaks of  $\text{Ni(OH)}_2$  after its coating on the surface of  $\text{C}/\text{ZnIn}_2\text{S}_4/\text{Fe}_2\text{O}_3$  (Fig. 2m). Furthermore, when in situ irradiated XPS measurement was performed on CZFN, binding energies of C1s, Zn2p, In3d and S2p peaks under visible light irradiation positively shift by 0.07, 0.17, 0.11 and 0.11 eV, respectively, while Fe2p and Ni2p peaks undergo negative shift (by 0.21 and 0.34 eV) compared to those in the dark (Fig. 2j-m and Fig. S6b,c). Such binding energy shifts

provide vivid evidences that photoexcited electrons move to  $\text{ZnIn}_2\text{S}_4$  and hollow C, while holes shift to  $\text{Fe}_2\text{O}_3$  and  $\text{Ni(OH)}_2$  during the photocatalytic process [48].

### 3.2. Photocatalytic performances analysis

For a more detailed investigation of the photocatalytic performance of CZFN, we synthesized a library of binary, ternary and quaternary counterparts for comparison, including  $\text{C}/\text{ZnIn}_2\text{S}_4$  (labeled as CZ), the step iii precursor of CZFN (Fig. 3a<sub>1</sub>);  $\text{C}/\text{Fe}_2\text{O}_3$  (labeled as CF) and  $\text{ZnIn}_2\text{S}_4/\text{Fe}_2\text{O}_3$  (labeled as ZF) with the deposition of  $\text{Fe}_2\text{O}_3$  on hollow C and  $\text{ZnIn}_2\text{S}_4$ , respectively (Fig. 3a<sub>2, a<sub>3</sub></sub>);  $\text{ZnIn}_2\text{S}_4/\text{Ni(OH)}_2$  (labeled as ZN) and  $\text{Fe}_2\text{O}_3/\text{Ni(OH)}_2$  (label as FN) with the encapsulation of  $\text{ZnIn}_2\text{S}_4$  and  $\text{Fe}_2\text{O}_3$  into  $\text{Ni(OH)}_2$ , respectively (Fig. 3a<sub>4, a<sub>5</sub></sub>);  $\text{C}/\text{ZnIn}_2\text{S}_4/\text{Fe}_2\text{O}_3$  (labeled as CZF), the step iv precursor of CZFN (Fig. 3a<sub>6</sub>);  $\text{C}/\text{ZnIn}_2\text{S}_4/\text{Ni(OH)}_2$  (labeled as CZN),  $\text{C}/\text{Fe}_2\text{O}_3/\text{Ni(OH)}_2$  (label as CFN) and  $\text{ZnIn}_2\text{S}_4/\text{Fe}_2\text{O}_3/\text{Ni(OH)}_2$  (labeled as ZFN) with the coating of CZ, CF and ZF with  $\text{Ni(OH)}_2$ , respectively (Fig. 3a<sub>7-9</sub>); and  $\text{C}/\text{Fe}_2\text{O}_3/\text{ZnIn}_2\text{S}_4/\text{Ni(OH)}_2$  (labeled as CFZN) in reverse stacking order of  $\text{ZnIn}_2\text{S}_4$  and  $\text{Fe}_2\text{O}_3$  relative to CZFN (Fig. 3a<sub>10</sub>). All the samples were adopted to conduct the photocatalytic reaction in the mixed vapor of  $\text{CO}_2$  and  $\text{H}_2\text{O}$  under visible light irradiation. As shown in Fig. 3b, there is no detectable product over zero-band-gap hollow C and wide-band-gap

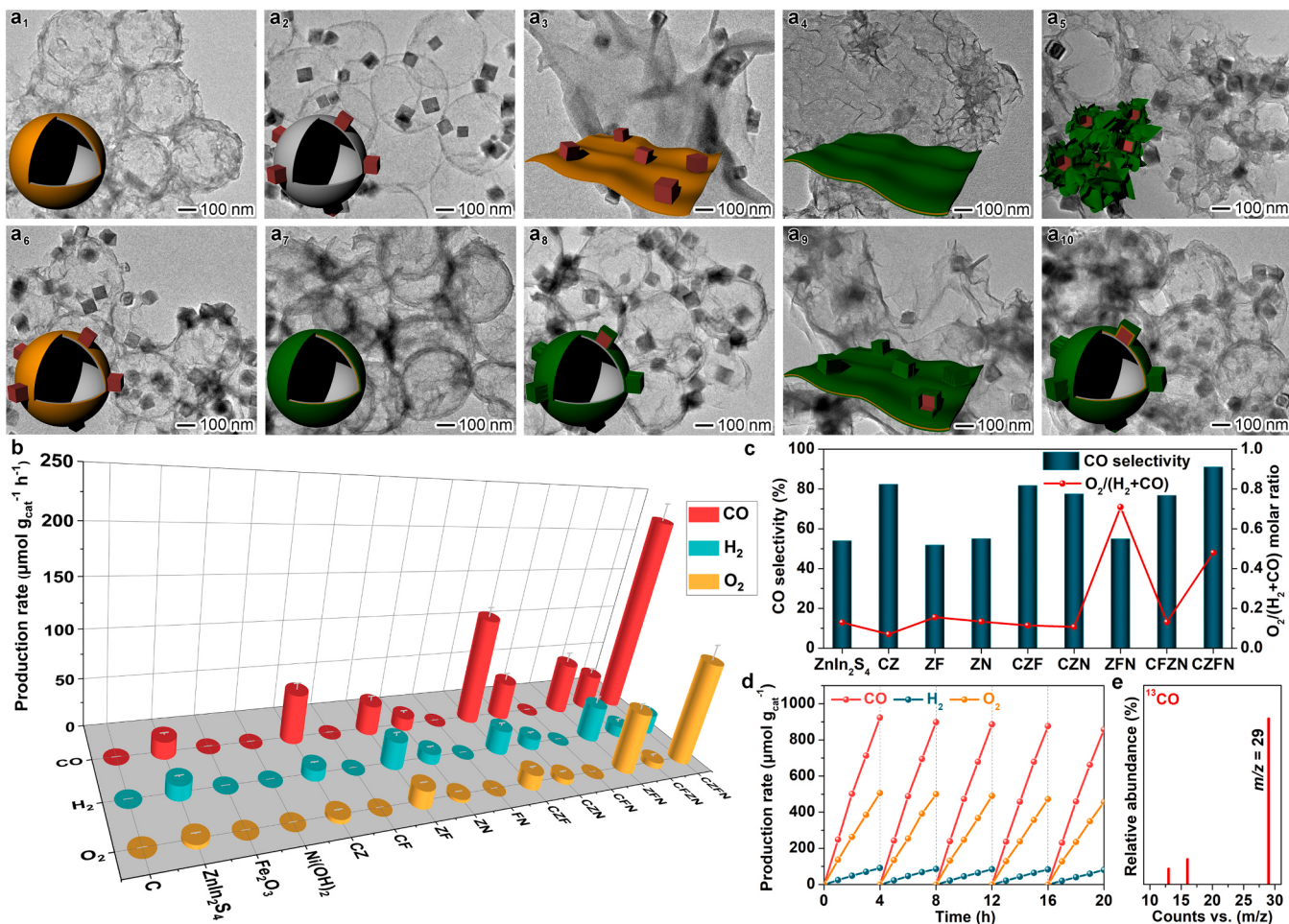


**Fig. 3.** Photocatalytic performance of CZFN and reference samples: (a) TEM images of binary, ternary and quaternary counterparts of CZFN: (a<sub>1</sub>) CZ, (a<sub>2</sub>) CF, (a<sub>3</sub>) ZF, (a<sub>4</sub>) ZN, (a<sub>5</sub>) FN, (a<sub>6</sub>) CZF, (a<sub>7</sub>) CZN, (a<sub>8</sub>) CFN, (a<sub>9</sub>) ZFN, and (a<sub>10</sub>) CFZN; (b) CO, H<sub>2</sub> and O<sub>2</sub> production rates under visible light irradiation in the absence of a sacrificial agent; (c) CO selectivity and molar ratio of oxidation product to reduction products; (d) recycling test of CZFN; (e) mass spectrum of <sup>13</sup>CO produced over CZFN.

Ni(OH)<sub>2</sub> owing to the mismatching between band energy and incident light. ZnIn<sub>2</sub>S<sub>4</sub> produces a trace amount of CO, H<sub>2</sub> and O<sub>2</sub>, while Fe<sub>2</sub>O<sub>3</sub> generates O<sub>2</sub> only in the presence of AgNO<sub>3</sub> electron scavenger because of unsuitable conduction band (CB) position for CO<sub>2</sub> and proton reduction half reaction (Fig. S7). Further introduction of hollow C elevates the CO yield of ZnIn<sub>2</sub>S<sub>4</sub> and simultaneously suppresses the side H<sub>2</sub> production, but cannot effectively improve the O<sub>2</sub> output of Fe<sub>2</sub>O<sub>3</sub>. In stark contrast, Ni(OH)<sub>2</sub> coating decreases the CO, H<sub>2</sub> and O<sub>2</sub> production of ZnIn<sub>2</sub>S<sub>4</sub>, but raises the O<sub>2</sub> evolution of Fe<sub>2</sub>O<sub>3</sub> only when AgNO<sub>3</sub> is added (Fig. 3b and Fig. S7). Namely, pairwise collaboration occurs in CZ and FN rather than CF and ZN. Furthermore, compared with CZ and FN, CZN and CFN exhibit no obvious enhancement in CO<sub>2</sub> reduction and H<sub>2</sub>O oxidation, again excluding the positive contribution of Ni(OH)<sub>2</sub> coverage and C supporting to the photoactivity of ZnIn<sub>2</sub>S<sub>4</sub> and Fe<sub>2</sub>O<sub>3</sub>, respectively. Coupling of ZnIn<sub>2</sub>S<sub>4</sub> and Fe<sub>2</sub>O<sub>3</sub> not only improves the evolution rates of CO and H<sub>2</sub>, but also enables the O<sub>2</sub> evolution in the absence of a sacrificial agent, confirming their synergistic effect in realizing overall redox reactions. Different from ZnIn<sub>2</sub>S<sub>4</sub> and Fe<sub>2</sub>O<sub>3</sub>, the photoactivity of ZF in CO<sub>2</sub> reduction and H<sub>2</sub>O oxidation can be upgraded when intergrating with either hollow C substrate or Ni(OH)<sub>2</sub> outer layer. Specifically, when both hollow C and Ni(OH)<sub>2</sub> are involved, CZFN delivers a maximal CO production rate of 230.7  $\mu\text{mol g}_{\text{cat}}^{-1} \text{h}^{-1}$  and O<sub>2</sub> production rate of 121.8  $\mu\text{mol g}_{\text{cat}}^{-1} \text{h}^{-1}$ , nearly 12.7 and 11.2 times higher than that of pristine ZnIn<sub>2</sub>S<sub>4</sub> and Fe<sub>2</sub>O<sub>3</sub>, respectively. The AQE of CZFN in CO generation is determined to be 1.98% at 420 nm.

Contrastingly, the CO and O<sub>2</sub> evolution rates of CFZN are remarkably inferior, even lower than those of ZF, explicitly evincing that the stacking sequence of ZnIn<sub>2</sub>S<sub>4</sub> and Fe<sub>2</sub>O<sub>3</sub> is critical to the photocatalytic enhancement.

The product selectivities over CZFN and control samples are compared in Fig. 3c. It can be clearly observed that carbon-containing samples exhibit apparently higher CO selectivities in reference to other samples, further verifying the pivotal role of hollow C in hindering the side proton reduction, in accordance with our previous report [35]. Specifically, CZFN achieves the highest CO selectivity of 90.9%, 1.7-fold that of blank ZnIn<sub>2</sub>S<sub>4</sub>. The activity and selectivity of CZFN in CO generation also transcend most of the reported ZnIn<sub>2</sub>S<sub>4</sub> based photocatalysts (Table S1). Furthermore, the molar ratios of oxidation product (O<sub>2</sub>) to reduction products (H<sub>2</sub> + CO) over ZnIn<sub>2</sub>S<sub>4</sub> involved samples were calculated. The O<sub>2</sub>/(H<sub>2</sub> + CO) ratio is close to 1: 2 stoichiometric ratio of the overall redox reactions (2CO<sub>2</sub>→2CO + O<sub>2</sub>; 2 H<sub>2</sub>O→2 H<sub>2</sub> + O<sub>2</sub>) in the case of CZFN, implying the well-balanced reduction and oxidation half reactions (Fig. 3c). As for other samples, the ratio is far below or above the theoretical value, suggesting the mismatched CO<sub>2</sub> reduction and H<sub>2</sub>O oxidation. To evaluate the photocatalytic stability of CZFN, five repeated cycles have been conducted with no pronounced activity decay after 20 h cycling tests (Fig. 3d). Moreover, the morphology, structure and composition of the used CZFN are well maintained when compared with the fresh one, confirming its excellent durability and reusability (Fig. S8 and S9). Inversely, photoactivity of ZF suffers from a

considerable decline under the same test conditions, convincing that the combination of C supporting and  $\text{Ni(OH)}_2$  coating protect the encapsulated semiconductor heterojunction against photocorrosion, leading to superior stability of CZFN (Fig. S10) [49]. To our surprise, when the

used CZFN after 5 cycles, which has been stored for 7 months, was re-tested for additional 15 cycles, the activity loss is also not evident during the discontinuous cyclic test, further evidencing its extremely long-term durability (Fig. S11). Besides,  $^{13}\text{C}$  isotopic labeling

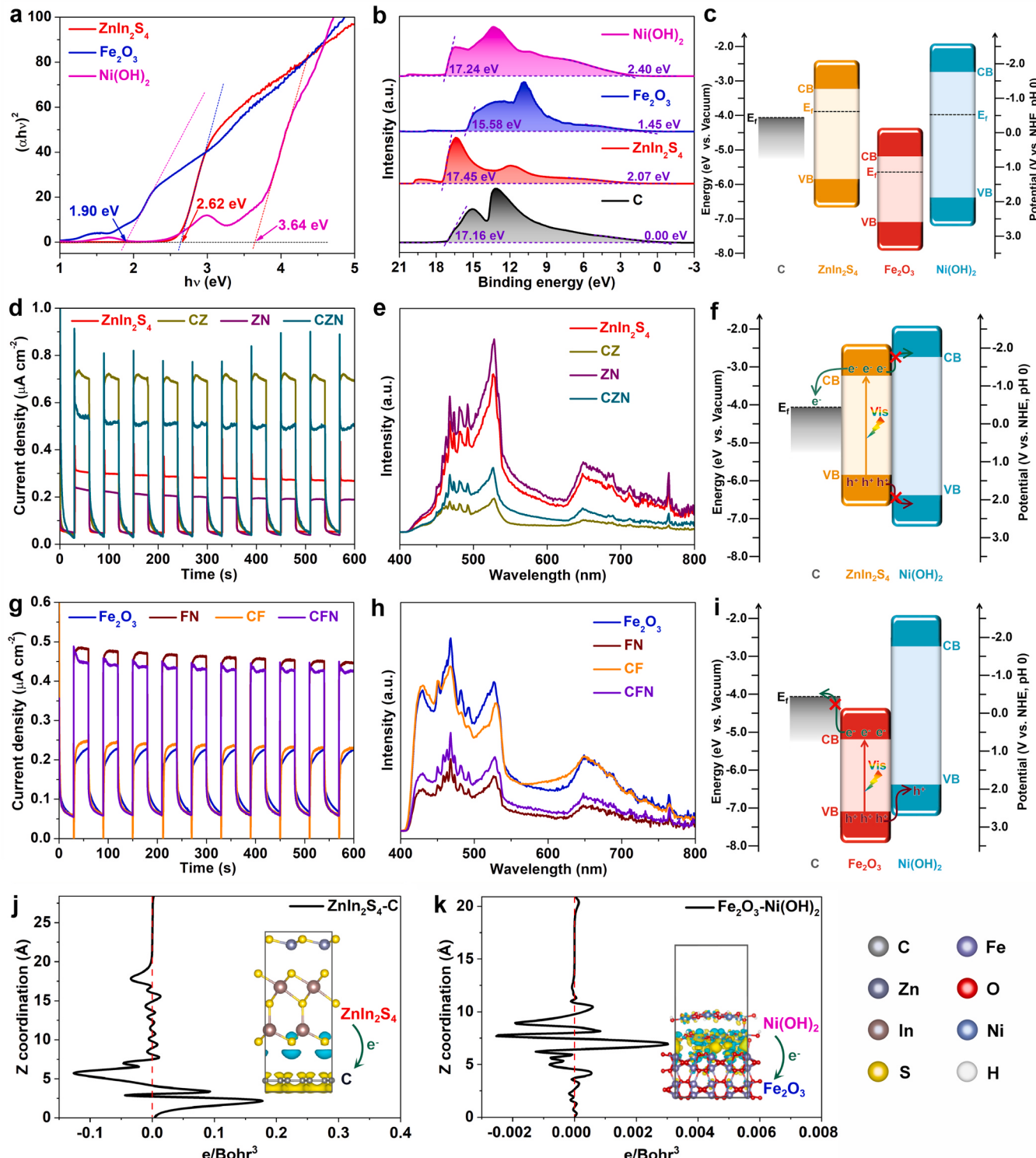


**Fig. 4.** Energy band alignments of the components involved in CZFN and charge transfer between them: (a) Tauc plots, (b) UPS spectra and (c) band alignments of hollow C,  $\text{ZnIn}_2\text{S}_4$ ,  $\text{Fe}_2\text{O}_3$  and  $\text{Ni(OH)}_2$ ; (d) photocurrent responses and (e) PL spectra of  $\text{ZnIn}_2\text{S}_4$ -containing samples; (f) schematic illustrating the charge transfer between  $\text{ZnIn}_2\text{S}_4$ , hollow C and  $\text{Ni(OH)}_2$ ; (g) photocurrent responses and (h) PL spectra of  $\text{Fe}_2\text{O}_3$ -containing samples; (i) schematic illustrating the charge transfer between  $\text{Fe}_2\text{O}_3$ , hollow C and  $\text{Ni(OH)}_2$ ; (j,k) profile of the plane-averaged differential charge density along the z-axis of (j)  $\text{ZnIn}_2\text{S}_4$ -C and (k)  $\text{Fe}_2\text{O}_3$ - $\text{Ni(OH)}_2$  as well as their corresponding simulated differential charge density distributions at the interfaces shown in the insets (the charge accumulation region is in yellow and the charge depletion region is in blue).

experiment has been performed to track to carbon source of reduction product, in which the GC-MS signal at  $m/z = 29$  strongly verifies that the generated CO indeed originates from the photoreduction of  $\text{CO}_2$  (Fig. 3e) [50]. Stirring speed in the photocatalytic reactor has little effect on the activity and selectivity of CZFN, inferring that catalytic reaction kinetics instead of mass transfer kinetics is the decisive factor of the photocatalytic performance (Fig. S12).

### 3.3. Charge transfer/separation kinetics analysis

To gain an in-depth insight into the improved photocatalytic performance of CZFN, band structures of the components involved were surveyed. According to Tauc plots derived from UV-vis diffuse reflectance spectra, the  $E_g$  of  $\text{ZnIn}_2\text{S}_4$ ,  $\text{Fe}_2\text{O}_3$  and  $\text{Ni(OH)}_2$  is estimated to be 2.62, 1.90 and 3.64 eV, respectively (Fig. 4a). Ultraviolet photoelectron spectroscopy (UPS) measurements further disclose that the work function of hollow C,  $\text{ZnIn}_2\text{S}_4$ ,  $\text{Fe}_2\text{O}_3$  and  $\text{Ni(OH)}_2$  is 4.06, 3.77, 5.64 and 3.98 eV, respectively, and the corresponding valence band maximum (VBM) is separately situated at 0.00, 2.07, 1.45 and 2.40 eV below the  $E_f$  (Fig. 4b). Namely, the  $E_f$  of hollow C,  $\text{ZnIn}_2\text{S}_4$ ,  $\text{Fe}_2\text{O}_3$  and  $\text{Ni(OH)}_2$  is located at  $-4.06$ ,  $-3.77$ ,  $-5.64$  and  $-3.98$  eV related to the vacuum level, which is equal to  $-0.44$ ,  $-0.73$ ,  $1.14$  and  $-0.52$  V (vs. NHE, pH 0), respectively [51]. As such, the valence band maximum (VBM) of  $\text{ZnIn}_2\text{S}_4$ ,  $\text{Fe}_2\text{O}_3$  and  $\text{Ni(OH)}_2$  is determined to be 1.34, 2.59 and 1.88 V vs. NHE, respectively. Then based on  $E_f$ , the corresponding conduction band minimum (CBM) is  $-1.28$ ,  $0.69$  and  $-1.76$  V vs. NHE, respectively. According to above discussion, energy band diagrams of C,  $\text{ZnIn}_2\text{S}_4$ ,  $\text{Fe}_2\text{O}_3$  and  $\text{Ni(OH)}_2$  are illustrated in Fig. 4c. Clearly, only narrow-band-gap  $\text{ZnIn}_2\text{S}_4$  and  $\text{Fe}_2\text{O}_3$  can be excited by visible light to produce photocarriers.

To evaluate the charge kinetics of the samples, we conducted photoelectrochemical and PL tests. Given the overlapped optical absorption range and approximate PL emission wavelength of  $\text{ZnIn}_2\text{S}_4$  and  $\text{Fe}_2\text{O}_3$ , to exclude their mutual interference, transient photocurrent responses of  $\text{ZnIn}_2\text{S}_4$ -containing samples without  $\text{Fe}_2\text{O}_3$  involved were employed to investigate the charge transfer between  $\text{ZnIn}_2\text{S}_4$ , hollow C and  $\text{Ni(OH)}_2$ . As shown in Fig. 4d, under chopped visible irradiation, compared with pristine  $\text{ZnIn}_2\text{S}_4$ , obvious enhancement in the photocurrent density is achieved by CZ, while there is a tremendous decline in the photocurrent response of ZN, evidencing that C supporter promotes charge separation in  $\text{ZnIn}_2\text{S}_4$ , while  $\text{Ni(OH)}_2$  overlayer induces aggravated charge recombination. Moreover, CZN demonstrates a photocurrent density even lower than that of CZ, further evincing the negative contribution of  $\text{Ni(OH)}_2$  coating to the charge separation in  $\text{ZnIn}_2\text{S}_4$ . The above statement is further confirmed by steady-state PL emission spectra (Fig. 4e), wherein the PL intensity of  $\text{ZnIn}_2\text{S}_4$  decreases in the order: ZN >  $\text{ZnIn}_2\text{S}_4$  > CZN > CZ, in line with the photocurrent enhancements. As illustrated in Fig. 4f, considering that the CB and valence band (VB) of  $\text{ZnIn}_2\text{S}_4$  are respectively lower and higher than those of  $\text{Ni(OH)}_2$ ,  $\text{Ni(OH)}_2$  can neither accept electrons nor holes from  $\text{ZnIn}_2\text{S}_4$  in terms of thermodynamics. As such,  $\text{Ni(OH)}_2$  coating obstructs the diffusion of charges generated by  $\text{ZnIn}_2\text{S}_4$ , thus inducing serious carrier recombination. Alternatively, photoelectrons migrate from the CB of  $\text{ZnIn}_2\text{S}_4$  to the  $E_f$  of hollow C driven by the energy difference between them. As for  $\text{Fe}_2\text{O}_3$ -containing samples without  $\text{ZnIn}_2\text{S}_4$  involved, the photocurrent densities follow the sequence:  $\text{Fe}_2\text{O}_3 \approx \text{CF} < \text{FN} \approx \text{CFN}$ , demonstrating that  $\text{Ni(OH)}_2$  instead of hollow C accelerates the charge separation in  $\text{Fe}_2\text{O}_3$  (Fig. 4g). Such a statement is further validated by the PL results, wherein obvious PL quenching of  $\text{Fe}_2\text{O}_3$  occurs after compounding with  $\text{Ni(OH)}_2$ , while there is no apparent decline in the PL intensities of CF and CFN when compared with  $\text{Fe}_2\text{O}_3$  and FN, respectively (Fig. 4h). As depicted in Fig. 4i, the CBM of  $\text{Fe}_2\text{O}_3$  is in lower position relative to the  $E_f$  of hollow C and CBM of  $\text{Ni(OH)}_2$ , making it impossible for the movement of photoelectrons from  $\text{Fe}_2\text{O}_3$  to them. Instead, holes migrate from  $\text{Fe}_2\text{O}_3$  to  $\text{Ni(OH)}_2$  with higher VB position. Based on above discussion, it can be concluded that C supporter and  $\text{Ni(OH)}_2$  outer layer selectively trap

photoelectrons and holes from  $\text{ZnIn}_2\text{S}_4$  and  $\text{Fe}_2\text{O}_3$ , respectively. Furthermore, electronic coupling between them and charge transfer direction at the interfaces were further reflected by DFT calculation. As visualized in Fig. 4j and k, intensive plane-averaged differential charge densities (DCDs)  $\Delta\rho$  oscillation along z direction highlights a noticeable charge redistribution at  $\text{ZnIn}_2\text{S}_4$ -C and  $\text{Fe}_2\text{O}_3$ - $\text{Ni(OH)}_2$  interfaces, and the corresponding differential charge density distributions manifest the  $\text{ZnIn}_2\text{S}_4$ -to-C and  $\text{Ni(OH)}_2$ -to- $\text{Fe}_2\text{O}_3$  electron transfer, reaffirming the interfacial charge transfer direction between them [52].

In terms of the samples with both  $\text{ZnIn}_2\text{S}_4$  and  $\text{Fe}_2\text{O}_3$  involved, ZF exhibits a significantly enhanced photocurrent density compared with the components involved, corroborating efficiently charge transfer between them (Fig. 5a). In light of the staggered band alignment between  $\text{ZnIn}_2\text{S}_4$  and  $\text{Fe}_2\text{O}_3$ , there are two possible mechanisms for the transfer and separation of photogenerated carriers in ZF: traditional Type-II and direct Z-scheme models. According to 5,5-dimethyl-1-pyrroline-N-oxide (DMPO) EPR spectra, under visible light irradiation, bare  $\text{ZnIn}_2\text{S}_4$  only generates DMPO- $\bullet\text{O}_2^-$  signal since its VBM is not positive enough to oxidize  $\text{H}_2\text{O}/\text{OH}$  to  $\bullet\text{OH}$ , while  $\text{Fe}_2\text{O}_3$  only produces DMPO- $\bullet\text{OH}$  signal since its CBM is not negative enough to reduce  $\text{O}_2$  to  $\bullet\text{O}_2^-$  (Fig. 5b,c). In stark contrast, both DMPO- $\bullet\text{O}_2^-$  and DMPO- $\bullet\text{OH}$  signals are generated by ZF, and the signal intensities are obviously strengthened in comparison with those of  $\text{ZnIn}_2\text{S}_4$  and  $\text{Fe}_2\text{O}_3$ . These results rule out the possibility of the formation of conventional Type-II heterojunction with the reason that neither signals attributing to DMPO- $\bullet\text{O}_2^-$  nor DMPO- $\bullet\text{OH}$  would be detected when photoelectrons transfer to the CB of  $\text{Fe}_2\text{O}_3$  along with the diffusion of holes in the opposite direction (Fig. 5d) [53]. Therefore, the charge transfer should follow the second scenario. That is the photoelectrons in the CB of  $\text{Fe}_2\text{O}_3$  recombine with holes in the VB of  $\text{ZnIn}_2\text{S}_4$ , leaving holes in the VB of  $\text{Fe}_2\text{O}_3$  and electrons in the CB of  $\text{ZnIn}_2\text{S}_4$  with stronger redox capabilities for  $\bullet\text{OH}$  and  $\bullet\text{O}_2^-$  generation, respectively (Fig. 5d). Based on aforementioned discussion, an S-scheme charge transfer mechanism is proposed (Fig. 5e). Given that  $\text{ZnIn}_2\text{S}_4$  possesses higher  $E_f$  relative to  $\text{Fe}_2\text{O}_3$ , upon their contact, to minimize their  $E_f$  difference, free electrons flow from  $\text{ZnIn}_2\text{S}_4$  to  $\text{Fe}_2\text{O}_3$ , giving rise to electron-deficient  $\text{ZnIn}_2\text{S}_4$  and electron-rich  $\text{Fe}_2\text{O}_3$ , in accordance with XPS results [54]. Consequently, an internal electric field (IEF) pointing from  $\text{ZnIn}_2\text{S}_4$  to  $\text{Fe}_2\text{O}_3$  creates at the interface together with the upward and downward band bending of  $\text{ZnIn}_2\text{S}_4$  and  $\text{Fe}_2\text{O}_3$ , respectively. Upon visible irradiation,  $\text{ZnIn}_2\text{S}_4$  and  $\text{Fe}_2\text{O}_3$  are excited to produce photoelectrons and holes. Under the combined effect of IEF and bent bands, weak CB electrons of  $\text{Fe}_2\text{O}_3$  transmit across the interface and recombine with the VB holes of  $\text{ZnIn}_2\text{S}_4$ . Meanwhile, strong  $\text{ZnIn}_2\text{S}_4$  electrons and  $\text{Fe}_2\text{O}_3$  holes are preserved for  $\text{CO}_2$  reduction and  $\text{H}_2\text{O}$  oxidation, respectively.

Compared with ZF, CZF and ZFN exhibit further increased photocurrent response, suggesting that both hollow C supporting and  $\text{Ni(OH)}_2$  coating accelerate the charge separation in ZF (Fig. 5f). When hollow C and  $\text{Ni(OH)}_2$  are simultaneously involved, CZFN delivers the highest photocurrent density, reflecting their synergy in maximizing the charge separation efficiency. By contrast, CFZN exhibits an inferior photocurrent as benchmarked against ZF, in consistence with the photocatalytic results. As depicted by electrochemical impedance spectroscopy (EIS) (Fig. 5g), the arc of Nyquist plot reduces in the order: CFZN > ZF > ZFN > CZF > CZFN, meaning the lowest interfacial charge-transfer resistance in CZFN. As expected, the average electron lifetimes ( $\tau_n$ ) of CZFN is obviously longer when compared with its counterparts (Fig. 5h), which was investigated by open-circuit voltage decay (OCVD) in the dark (Fig. S13), supporting that more efficient charge separation and transfer exerts a pronounced effect on the prolonged  $\tau_n$ . Taking the architectures of the samples into consideration, electron migration from  $\text{ZnIn}_2\text{S}_4$  to C supporter is facilitated by the large-area C- $\text{ZnIn}_2\text{S}_4$  interface in CZF, while hole transportation from  $\text{Fe}_2\text{O}_3$  core to  $\text{Ni(OH)}_2$  shell is smoothed by their full contact in ZFN. For CZFN, the  $\text{ZnIn}_2\text{S}_4 \rightarrow \text{C}$  electron flow and  $\text{Fe}_2\text{O}_3 \rightarrow \text{Ni(OH)}_2$  hole movement occurs in parallel, contributing to well-balanced charge transport. As for CFZN, though

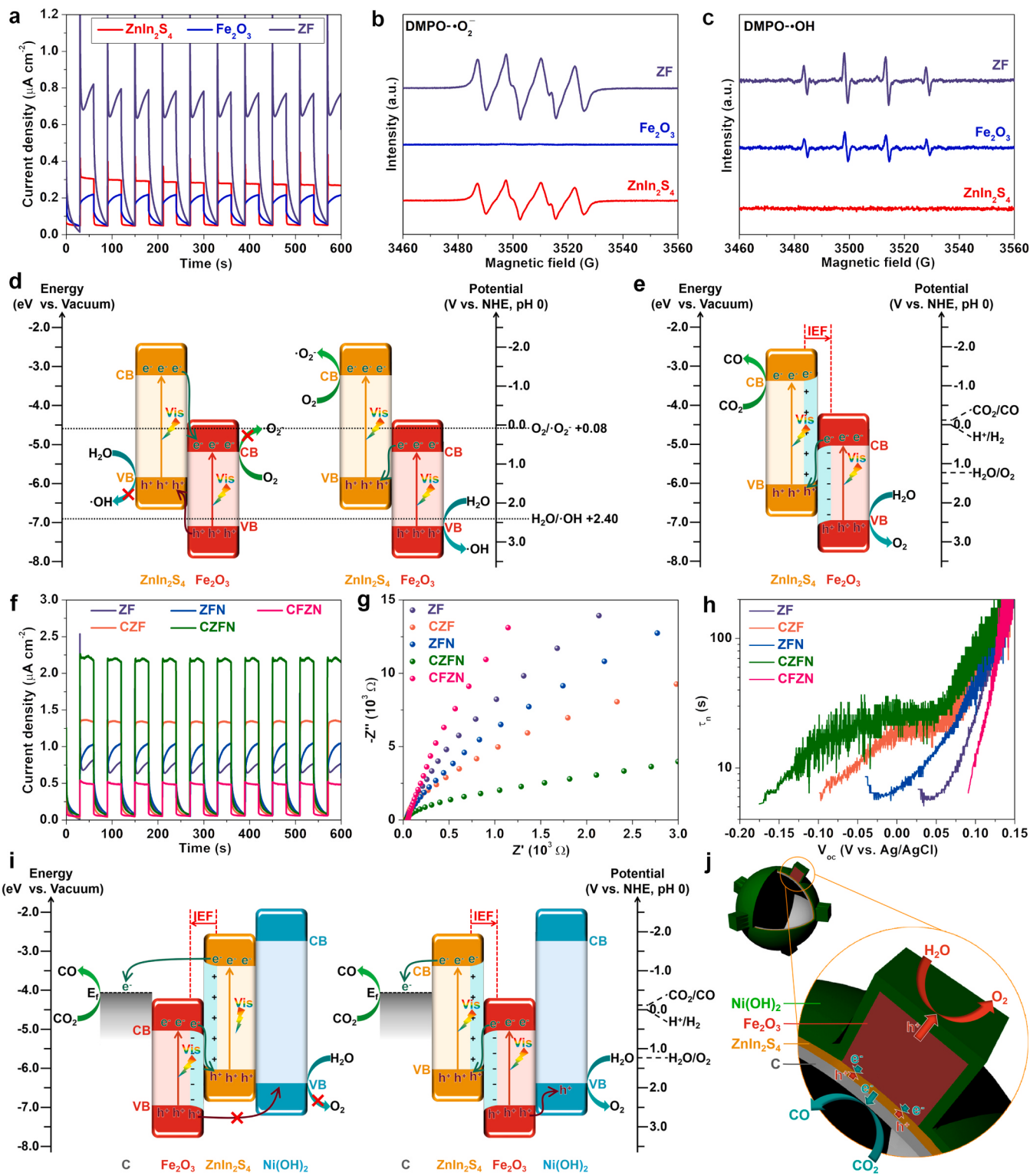


**Fig. 5.** Charge separation/transfer kinetics analysis of CZFN and reference samples: (a) photocurrent responses, (b) DMPO-·O<sub>2</sub><sup>-</sup> and (c) DMPO-OH EPR spectra of ZnIn<sub>2</sub>S<sub>4</sub>, Fe<sub>2</sub>O<sub>3</sub> and ZF; (d) Type-II and direct Z-scheme charge transfer pathways between ZnIn<sub>2</sub>S<sub>4</sub> and Fe<sub>2</sub>O<sub>3</sub>; (e) proposed S-scheme charge transfer mechanism of ZF; (f) photocurrent responses, (g) EIS Nyquist plots, and (h) average electron lifetimes of CZFN and reference samples; (i,j) energy band diagrams and photocatalytic reaction mechanisms of CFZN and CZFN.

photoelectrons migration from ZnIn<sub>2</sub>S<sub>4</sub> to C substrate is enabled by the interfacial contact between them, hole transmission from Fe<sub>2</sub>O<sub>3</sub> to Ni(OH)<sub>2</sub> outer layer is blocked by ZnIn<sub>2</sub>S<sub>4</sub> interlayer. The sluggish diffusion out of holes inevitably causes unbalanced carrier utilization and serious charge recombination (Fig. 5i). Based on above analysis results,

the reaction mechanism of CZFN is illustrated in Fig. 5i and j. Under illumination, weak Fe<sub>2</sub>O<sub>3</sub> electrons drift across the Fe<sub>2</sub>O<sub>3</sub>-ZnIn<sub>2</sub>S<sub>4</sub> interface and recombine with powerless ZnIn<sub>2</sub>S<sub>4</sub> holes. Concurrently, strong ZnIn<sub>2</sub>S<sub>4</sub> electrons diffuse to inner hollow C for CO<sub>2</sub> reduction, and powerful Fe<sub>2</sub>O<sub>3</sub> holes transmit to outer Ni(OH)<sub>2</sub> for H<sub>2</sub>O oxidation. The

inward and outward migration of photocreated electrons and holes in opposite directions matches well with results of in-situ irradiated XPS, accounting for thorough charge separation and thus the highest photoactivity of CZFN.

#### 3.4. Surface reaction dynamics analysis

Apart from charge separation/transfer kinetics, surface reaction dynamics were further explored to unravel the origin of photocatalytic enhancements. Fig. 6a shows the linear sweep voltammetry (LSV) curves for O<sub>2</sub> evolution conducted in KOH electrolyte, in which ZFN and CZFN display lower onset potentials and higher current densities in reference to ZF and CZF, manifesting that Ni(OH)<sub>2</sub> coverage enriches the reaction sites for H<sub>2</sub>O oxidation [55]. When LSV curves are collected in Ar and CO<sub>2</sub>-saturated KHCO<sub>3</sub> electrolyte, the higher current density in CO<sub>2</sub> atmosphere relative to that in Ar atmosphere can be attributed to the cathodic current generated by CO<sub>2</sub> reduction (Fig. 6b) [56]. Compared to ZF and ZFN, CZF and CZFN exhibit larger CO<sub>2</sub> reduction current densities, affirming that C substrate offers highly active centres for CO<sub>2</sub> fixation [57]. Fig. 6c presents the CO<sub>2</sub> adsorption isotherms of CZFN and its components at 298 K. Obviously, in line with the BET data, CZFN

displays a CO<sub>2</sub> adsorption capacity higher than those of ZnIn<sub>2</sub>S<sub>4</sub>, Fe<sub>2</sub>O<sub>3</sub> and Ni(OH)<sub>2</sub>, but lower than that of hollow C, further validating that C supporter is the decisive component adsorbing CO<sub>2</sub> molecules, mainly owing to its porous nature and large specific surface area.

To in-depth understand the reaction pathway and underlying reasons of the increased reactivity in CO<sub>2</sub> photoreduction, in situ diffuse reflectance infrared Fourier transform spectroscopy (DRIFTS) was carried out for precisely tracking the reactive intermediates during the CO<sub>2</sub> reduction on the surface of ZFN and CZFN. As shown in Fig. 6d and e, for both samples, there is no obvious DRIFTS signal in the dark. Irradiated by visible light, obvious adsorption bands can be recorded by ZFN, including bidentate carbonate (b-CO<sub>3</sub><sup>2-</sup>: 1651, 1575 and 1557 cm<sup>-1</sup>), monodentate carbonate (m-CO<sub>3</sub><sup>2-</sup>: 1635, 1472, 1456 and 1292 cm<sup>-1</sup>), bicarbonate (HCO<sub>3</sub><sup>-</sup>: 1433, 1417, 1395 cm<sup>-1</sup>), carboxylate (•CO<sub>2</sub>: 1682, 1668 and 1248 cm<sup>-1</sup>), and the intensities of which gradually increase with the elongation of irradiation time [58–60]. Especially, carboxyl (\*COOH) signal is detected at 1540, 1521, 1506 and 1145 cm<sup>-1</sup>, which is regarded as the key intermediate during the CO<sub>2</sub>-to-CO reduction. As for CZFN, the intensities of absorption bands assigned to \*COOH, b-CO<sub>3</sub><sup>2-</sup>, m-CO<sub>3</sub><sup>2-</sup>, HCO<sub>3</sub><sup>-</sup> and •CO<sub>2</sub> increase more dramatically under the same irradiation time when compared with ZFN. Additionally, a new

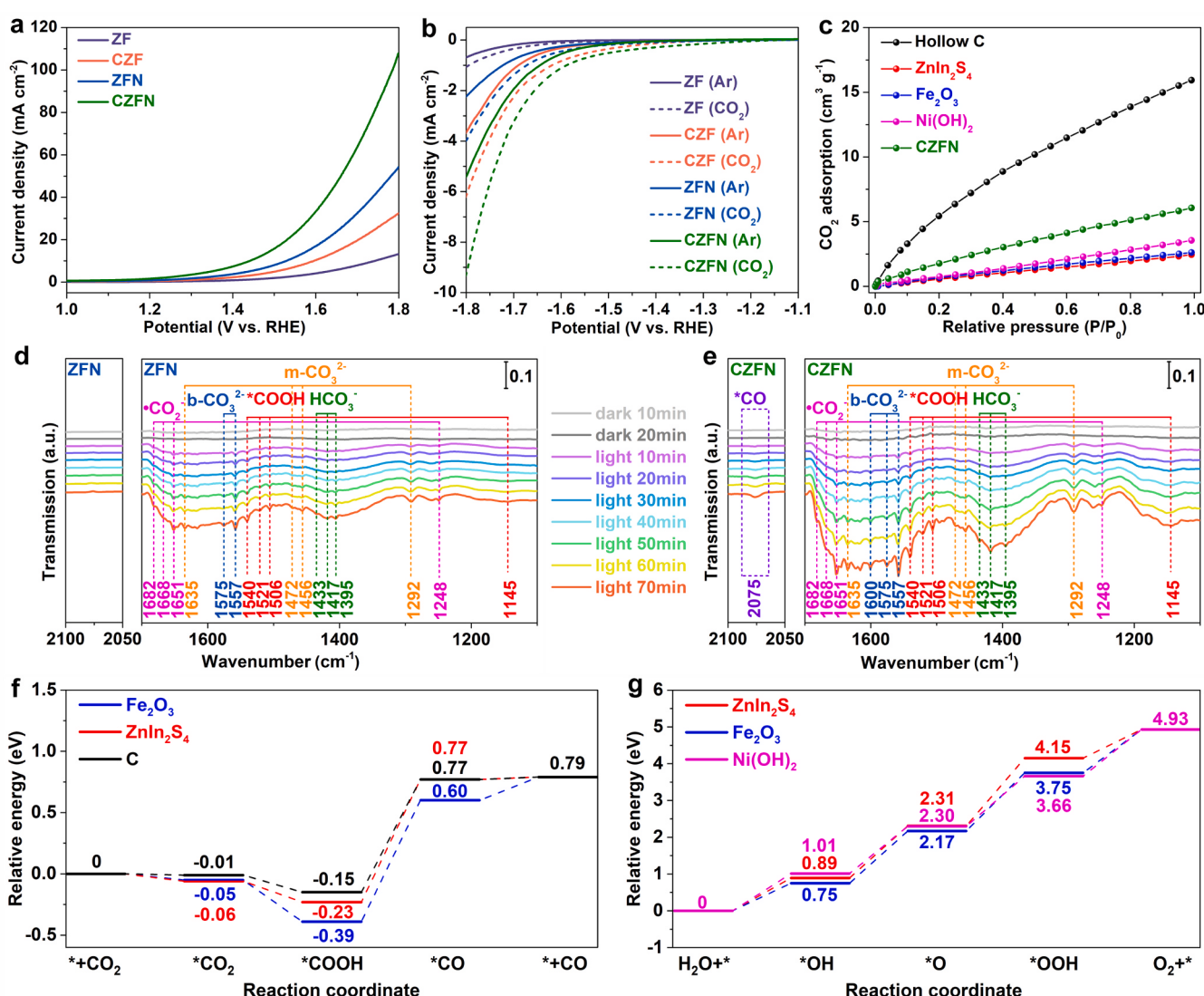


Fig. 6. Surface reaction dynamics analysis of CZFN and reference samples: (a,b) LSV curves for (a) CO<sub>2</sub> reduction and (b) O<sub>2</sub> evolution; (c) CO<sub>2</sub> adsorption isotherms; (d) in situ DRIFTS spectra of CO<sub>2</sub> reduction with H<sub>2</sub>O over (d) ZFN and (e) CZFN; (f) free energy diagrams of CO<sub>2</sub>-to-CO reduction on ZnIn<sub>2</sub>S<sub>4</sub>, Fe<sub>2</sub>O<sub>3</sub> and hollow C; (g) free energy diagrams of H<sub>2</sub>O-to-O<sub>2</sub> oxidation on ZnIn<sub>2</sub>S<sub>4</sub>, Fe<sub>2</sub>O<sub>3</sub> and Ni(OH)<sub>2</sub>.

band appearing at  $2075\text{ cm}^{-1}$  is indicated for the formation of  $^*\text{CO}$ , which is consistent with its superior activity in CO formation [61]. Based on the DRIFTS results, the plausible  $\text{CO}_2$  reduction pathway is  $\text{CO}_2 \rightarrow ^*\text{CO}_2 \rightarrow ^*\text{COOH} \rightarrow ^*\text{CO} \rightarrow \text{CO}$ , which is more favorable when C substrate is introduced into ZFN.

To further gain insight into the  $\text{CO}_2$  photoreduction mechanism on CZFN, DFT calculations were performed to reveal the pivotal role of hollow C in achieving both the high activity and selectivity in CO production. Fig. 6f (also Fig. S14a) shows the free energy diagrams for  $\text{CO}_2$ -to-CO reduction on  $\text{ZnIn}_2\text{S}_4$ ,  $\text{Fe}_2\text{O}_3$  and hollow C, as well as the optimized configurations of the intermediates adsorbed on the surface. For all the models, the key step for CO production is the coupling of  $^*\text{COOH}$  with a proton/electron pair to generate  $^*\text{CO}$ . Clearly, in the case of hollow C, the free-energy change ( $\Delta G$ ) value for this step is 0.92 eV, smaller than those of  $\text{ZnIn}_2\text{S}_4$  (1.00 eV) and  $\text{Fe}_2\text{O}_3$  (0.99 eV), demonstrating that C supporter lowers the energy barrier for CO formation. We also compare the Gibbs free energy changes during the  $\text{H}_2\text{O}$  oxidation to  $\text{O}_2$  on  $\text{ZnIn}_2\text{S}_4$ ,  $\text{Fe}_2\text{O}_3$  and  $\text{Ni(OH)}_2$  surface. As displayed in Fig. 6g (also Fig. S14b),  $\text{OOH}^*$  formation is the endergonic rate-limiting step, and the free energy barrier  $\Delta G_{\text{OOH}^*}$  for  $\text{Ni(OH)}_2$  (1.36 eV) is lower than those of  $\text{ZnIn}_2\text{S}_4$  (1.84 eV) and  $\text{Fe}_2\text{O}_3$  (1.58 eV). Hence, the presence of  $\text{Ni(OH)}_2$  overlayer is more beneficial for  $\text{H}_2\text{O}$  oxidation in term of lower energy barrier. Based on above experimental and theoretical results, it is very comprehensive to conclude that the inner C and outer  $\text{Ni(OH)}_2$  layers of CZFN separately co-catalyze the  $\text{CO}_2$  reduction and  $\text{H}_2\text{O}$  oxidation in a more favorable way.

#### 4. Conclusion

In summary, a hollow multi-shelled nanoreactor with S-scheme heterojunction sandwiched between spatially separated layered double-cocatalysts is constructed via the step-by-step deposition of  $\text{ZnIn}_2\text{S}_4$ ,  $\text{Fe}_2\text{O}_3$  and  $\text{Ni(OH)}_2$  on hollow carbon spheres. In the smart design, IEF and band bending in the inserted  $\text{ZnIn}_2\text{S}_4/\text{Fe}_2\text{O}_3$  S-scheme heterojunction promote the recombination of carriers with lower redox abilities, and separate powerful photoelectrons and holes in  $\text{ZnIn}_2\text{S}_4$  and  $\text{Fe}_2\text{O}_3$ , which move to the inner carbon supporter and outer  $\text{Ni(OH)}_2$  overlayer for  $\text{CO}_2$  reduction and  $\text{H}_2\text{O}$  oxidation inside and outside the chamber, respectively. Comprehensive experimental and theoretical investigation reveals that the large-area contact and strong electronic coupling between the components smoothen the interfacial charge transfer and boost the electron-hole separation. Meanwhile, C substrates and  $\text{Ni(OH)}_2$  outer layers afford highly active sites for  $\text{CO}_2$  reduction and  $\text{H}_2\text{O}$  oxidation, reduce the rate-determining barrier for CO formation and  $\text{O}_2$  evolution, and suppress the occurrence of side proton reduction and undesirable photocorrosion on the semiconductor surface. Benefiting from the simultaneous optimization of charge kinetics and surface reactivity, the quaternary nanoreactor not only delivers a benchmarked activity ( $230.7\text{ }\mu\text{mol g}^{-1}\text{ h}^{-1}$ ) and selectivity (90.9%) for CO production, markedly superior to a series of counterparts, but also realizes the stoichiometric production of reduction and oxidation products. The results obtained in this study provide a general and unique strategy to balance the separation, transfer and consumption of electrons and holes for overall redox reactions, and inspire the developments of two-dimensional earth-abundant wrapping cocatalysts for artificial photosynthesis.

#### CRediT authorship contribution statement

**Xingwei Zhang:** Conceptualization, Investigation, Data curation, Writing – original draft. **Yili Song:** Software, Calculus analysis, Validation. **Xiangyue Niu:** Conceptualization, Investigation. **Xinyuan Lin:** Investigation, Data curation. **Shuxian Zhong:** Investigation. **Hongjun Lin:** Resources. **Botao Teng:** Methodology, Validation, Funding acquisition. **Song Bai:** Conceptualization, Formal analysis, Supervision, Writing – review & editing, Funding acquisition, Project administration.

#### Declaration of Competing Interest

The authors declare that they have no known competing financial interests or personal relationships that could have appeared to influence the work reported in this paper.

#### Data Availability

Data will be made available on request.

#### Acknowledgements

This work was financially supported by the National Natural Science Foundation of China (No. 21603191 and 22372120), Zhejiang Provincial Natural Science Foundation of China (No. LY20B030003 and LQ16B010001), Key Research and Development Program of Zhejiang Province (No. 2022C03069), Public Welfare Technology Application Research Plan Project of Zhejiang Province (Analysis Test Item, No. 2017C37024), Foundation of Science and Technology Bureau of Jinhua (No. 20204185), and Self-Topic Fund of Zhejiang Normal University.

#### Appendix A. Supporting information

Supplementary data associated with this article can be found in the online version at doi:10.1016/j.apcatb.2023.123445.

#### References

- [1] A. Wagner, C. Sahm, E. Reisner, Towards molecular understanding of local chemical environment effects in electro- and photocatalytic  $\text{CO}_2$  reduction, *Nat. Catal.* 3 (2020) 775–786, <https://doi.org/10.1038/s41929-020-00512-x>.
- [2] W. Tu, Y. Zhou, Z. Zou, Photocatalytic conversion of  $\text{CO}_2$  into renewable hydrocarbon fuels: state-of-the-art accomplishment, challenges, and prospects, *Adv. Mater.* 26 (2014) 4607–4626, <https://doi.org/10.1002/adma.201400087>.
- [3] S. Haberreutinger, L. Schmidt-Mende, J. Stolarczyk, Photocatalytic reduction of  $\text{CO}_2$  on  $\text{TiO}_2$  and other semiconductors, *Angew. Chem. Int. Ed.* 52 (2013) 7372–7408, <https://doi.org/10.1002/anie.201207199>.
- [4] K. Li, B. Peng, T. Peng, Recent advances in heterogeneous photocatalytic  $\text{CO}_2$  conversion to solar fuels, *ACS Catal.* 6 (2016) 7485–7527, <https://doi.org/10.1021/acscatal.6b02089>.
- [5] S. Bai, J. Jiang, Q. Zhang, Y. Xiong, Steering charge kinetics in photocatalysis: intersection of materials syntheses, characterization techniques and theoretical simulations, *Chem. Soc. Rev.* 44 (2015) 2893–2939, <https://doi.org/10.1039/c5cs00064e>.
- [6] K. Jacek, B. Santanu, P. Lakshminarayana, F. Jochen, Challenges and prospects in solar water splitting and  $\text{CO}_2$  reduction with inorganic and hybrid nanostructures, *ACS Catal.* 8 (2018) 3602–3635, <https://doi.org/10.1021/acscatal.8b00791>.
- [7] B. Tomasz, W. Szymon, D. Angela, A. Michele, M. Wojciech, Photocatalytic carbon dioxide reduction at p-type copper(I) iodide, *ChemSusChem* 9 (2016) 2933–2938, <https://doi.org/10.1002/cssc.201600289>.
- [8] Y. He, H. Rao, K. Song, J. Li, Y. Yu, Y. Lou, C. Li, Y. Han, Z. Shi, S. Feng, 3D hierarchical  $\text{ZnIn}_2\text{S}_4$  nanosheets with rich Zn vacancies boosting photocatalytic  $\text{CO}_2$  reduction, *Adv. Funct. Mater.* 29 (2019), 1905153, <https://doi.org/10.1002/adfm.201905153>.
- [9] Y. Wang, X. Shang, J. Shen, Z. Zhang, D. Wang, J. Lin, J. Wu, X. Fu, X. Wang, C. Li, Direct and indirect Z-scheme heterostructure-coupled photosystem enabling cooperation of  $\text{CO}_2$  reduction and  $\text{H}_2\text{O}$  oxidation, *Nat. Commun.* 11 (2020), 3043, <https://doi.org/10.1038/s41467-020-16742-3>.
- [10] Y. Wang, Z. Zhang, L. Zhang, Z. Luo, J. Shen, H. Lin, J. Long, J. Wu, X. Fu, X. Wang, C. Li, Visible-light driven overall conversion of  $\text{CO}_2$  and  $\text{H}_2\text{O}$  to  $\text{CH}_4$  and  $\text{O}_2$  on 3D- $\text{SiC@2D-MoS}_2$  heterostructure, *J. Am. Chem. Soc.* 140 (2018) 14595–14598, <https://doi.org/10.1021/jacs.8b09344>.
- [11] S. Bai, J. Ge, L. Wang, M. Gong, M. Deng, Q. Kong, L. Song, J. Jiang, Q. Zhang, Y. Luo, Y. Xie, Y. Xiong, A unique semiconductor-metal-graphene stack design to harness charge flow for photocatalysis, *Adv. Mater.* 26 (2014) 5689–5695, <https://doi.org/10.1002/adma.201401817>.
- [12] Z. Wei, W. Wang, W. Li, X. Bai, J. Zhao, E. Tse, D. Phillips, Y. Zhu, Steering electron-hole migration pathways using oxygen vacancies in tungsten oxides to enhance their photocatalytic oxygen evolution performance, *Angew. Chem. Int. Ed.* 60 (2021) 8236–8242, <https://doi.org/10.1002/anie.202016170>.
- [13] Q. Xu, L. Zhang, B. Cheng, J. Fan, J. Yu, S-scheme heterojunction photocatalyst, *Chem* 6 (2020) 1543–1559, <https://doi.org/10.1016/j.chempr.2020.06.010>.
- [14] L. Zhang, J. Zhang, H. Yu, J. Yu, Emerging S-scheme photocatalyst, *Adv. Mater.* 34 (2022), 2107668, <https://doi.org/10.1002/adma.202107668>.
- [15] F. Xu, K. Meng, B. Cheng, S. Wang, J. Xu, J. Yu, Unique S-scheme heterojunctions in self-assembled  $\text{TiO}_2/\text{CsPbBr}_3$  hybrids for  $\text{CO}_2$  photoreduction, *Nat. Commun.* 11 (2020), 4613, <https://doi.org/10.1038/s41467-020-18350-7>.

[16] L. Wang, B. Zhu, J. Zhang, J. Ghasemi, M. Mousavi, J. Yu, S-scheme heterojunction photocatalysts for CO<sub>2</sub> reduction, *Matter* 5 (2022) 4187–4211, <https://doi.org/10.1016/j.matt.2022.09.009>.

[17] Y. Xi, W. Chen, W. Dong, Z. Fan, K. Wang, Y. Shen, G. Tu, S. Zhong, S. Bai, Engineering an interfacial facet of S-scheme heterojunction for improved photocatalytic hydrogen evolution by modulating the internal electric field, *ACS Appl. Mater. Interfaces* 13 (2021) 39491–39500, <https://doi.org/10.1021/acsami.1c11233>.

[18] L. Wang, C. Bie, J. Yu, Challenges of Z-scheme photocatalytic mechanisms, *Trends Chem.* 11 (2022) 973–983, <https://doi.org/10.1016/j.trechm.2022.08.008>.

[19] X. Li, J. Yu, M. Jaroniec, X. Chen, Cocatalysts for selective photoreduction of CO<sub>2</sub> into solar fuels, *Chem. Rev.* 119 (2019) 3962–4179, <https://doi.org/10.1021/acs.chemrev.8b00400>.

[20] J. Yang, D. Wang, H. Han, C. Li, Roles of cocatalysts in photocatalysis and photoelectrocatalysis, *Acc. Chem. Res.* 46 (2013) 1900–1909, <https://doi.org/10.1021/ar300227e>.

[21] J. Ran, M. Jaroniec, S. Qiao, Cocatalysts in semiconductor-based photocatalytic CO<sub>2</sub> reduction: achievements, challenges, and opportunities, *Adv. Mater.* 30 (2018), 1704649, <https://doi.org/10.1002/adma.201704649>.

[22] A. Meng, L. Zhang, B. Cheng, J. Yu, Dual cocatalysts in TiO<sub>2</sub> photocatalysis, *Adv. Mater.* 31 (2019) 1807660, <https://doi.org/10.1002/adma.201807660>.

[23] B. Qiu, M. Du, Y. Ma, Q. Zhu, M. Xing, J. Zhang, Integration of redox cocatalysts for artificial photosynthesis, *Energy Environ. Sci.* 14 (2021) 5260–5288, <https://doi.org/10.1039/dlee02359d>.

[24] Z. Wang, Y. Luo, T. Hisatomi, J. Vequizo, S. Suzuki, S. Chen, M. Nakabayashi, L. Lin, Z. Pan, N. Kariya, A. Yamakata, N. Shibata, T. Takata, K. Teshima, K. Domen, Sequential cocatalyst decoration on BaTaO<sub>4</sub>N towards highly-active Z-scheme water splitting, *Nat. Commun.* 12 (2021), 1005, <https://doi.org/10.1038/s41467-021-21284-3>.

[25] R. Li, F. Zhang, D. Wang, J. Yang, M. Li, J. Zhu, X. Zhou, H. Han, C. Li, Spatial separation of photogenerated electrons and holes among {010} and {110} crystal facets of BiVO<sub>4</sub>, *Nat. Commun.* 4 (2013), 1432, <https://doi.org/10.1038/ncomms2401>.

[26] G. Yang, S. Wang, Y. Wu, H. Zhou, W. Zhao, S. Zhong, L. Liu, S. Bai, Spatially separated redox cocatalysts on ferroelectric nanoplates for improved piezophotocatalytic CO<sub>2</sub> reduction and H<sub>2</sub>O oxidation, *ACS Appl. Mater. Interfaces* 15 (2023) 14228–14239, <https://doi.org/10.1021/acsami.2c20685>.

[27] J. Fu, K. Jiang, X. Qiu, J. Yu, M. Liu, Product selectivity of photocatalytic CO<sub>2</sub> reduction reactions, *Mater. Today* 32 (2022) 222–243, <https://doi.org/10.1016/j.mattod.2019.06.009>.

[28] B. Weng, M. Qi, C. Han, Z. Tang, Y. Xu, Photocorrosion inhibition of semiconductor-based photocatalysts: basic principle, current development, and future perspective, *ACS Catal.* 9 (2019) 4642–4687, <https://doi.org/10.1021/acs.catal.9b00313>.

[29] S. Chen, D. Huang, P. Xu, W. Xue, L. Lei, M. Cheng, R. Wang, X. Liu, R. Deng, Semiconductor-based photocatalysts for photocatalytic and photoelectrochemical water splitting: will we stop with photocorrosion? *J. Mater. Chem. A* 8 (2020) 2286–2322, <https://doi.org/10.1039/C9TA12799B>.

[30] C. Han, N. Zhang, Y. Xu, Structural diversity of graphene materials and their multifarious roles in heterogeneous photocatalysis, *Nano Today* 11 (2016) 351–372, <https://doi.org/10.1016/j.nantod.2016.05.008>.

[31] F. Xu, K. Meng, B. Zhu, H. Liu, J. Xu, J. Yu, Graphdiyne: A new photocatalytic CO<sub>2</sub> reduction cocatalyst, *Adv. Funct. Mater.* 29 (2019), 1904256, <https://doi.org/10.1002/adfm.201904256>.

[32] J. Ran, B. Zh, S. Qiao, Phosphorene Co-catalyst advancing highly efficient visible-light photocatalytic hydrogen production, *Angew. Chem. Int. Ed.* 56 (2017) 10373–10377, <https://doi.org/10.1002/anie.201703827>.

[33] T. Su, C. Men, L. Chen, B. Chu, X. Luo, H. Ji, J. Chen, Z. Qin, Sulfur vacancy and Ti<sub>3</sub>C<sub>2</sub>T<sub>x</sub> cocatalyst synergistically boosting interfacial charge transfer in 2D/2D Ti<sub>3</sub>C<sub>2</sub>T<sub>x</sub>/ZnIn<sub>2</sub>S<sub>4</sub> heterostructure for enhanced photocatalytic hydrogen evolution, *Adv. Sci.* 9 (2022), 2103715, <https://doi.org/10.1002/advs.202103715>.

[34] S. Bai, L. Wang, X. Chen, J. Du, Y. Xiong, Chemically exfoliated metallic MoS<sub>2</sub> nanosheets: a promising supporting co-catalyst for enhancing the photocatalytic performance of TiO<sub>2</sub> nanocrystals, *Nano Res* 8 (2015) 175–183, <https://doi.org/10.1007/s12274-014-0606-9>.

[35] Z. Li, W. Zhou, Y. Tang, X. Tan, Y. Zhang, Z. Geng, Y. Guo, L. Liu, T. Yu, J. Ye, Insights into the operation of noble-metal-free cocatalyst 1T-WS<sub>2</sub>-decorated Zn<sub>0.5</sub>Cd<sub>0.5</sub>S for enhanced photocatalytic hydrogen evolution, *ChemSusChem* 14 (2021) 4752–4763, <https://doi.org/10.1002/cssc.202101670>.

[36] Q. Liu, S. Wang, W. Mo, Y. Zheng, Y. Xu, G. Yang, S. Zhong, J. Ma, D. Liu, S. Bai, Emerging stacked photocatalyst design enables spatially separated Ni(OH)<sub>2</sub> redox cocatalysts for overall CO<sub>2</sub> reduction and H<sub>2</sub>O oxidation, *Small* 18 (2022), 2104681, <https://doi.org/10.1002/smll.202104681>.

[37] G. Zhang, S. Zang, X. Wang, Layered Co(OH)<sub>2</sub> deposited polymeric carbon nitrides for photocatalytic water oxidation, *ACS Catal.* 5 (2015) 941–947, <https://doi.org/10.1021/cs502002u>.

[38] Y. Su, Z. Song, W. Zhu, Q. Mu, X. Yuan, Y. Lian, H. Cheng, Z. Deng, M. Chen, W. Yin, Y. Peng, Visible-light photocatalytic CO<sub>2</sub> reduction using metal-organic framework derived Ni(OH)<sub>2</sub> nanocages: a synergy from multiple light reflection, static charge transfer, and oxygen vacancies, *ACS Catal.* 11 (2021) 345–354, <https://doi.org/10.1021/acscatal.0c04020>.

[39] A. Li, T. Wang, X. Chang, Z. Zhao, C. Li, Z. Huang, P. Yang, G. Zhou, J. Gong, Tunable syngas production from photocatalytic CO<sub>2</sub> reduction with mitigated charge recombination driven by spatially separated cocatalysts, *Chem. Sci.* 9 (2018) 5334, <https://doi.org/10.1039/c8sc01812j>.

[40] Z. Leongab, H. Yang, Porous carbon hollow spheres synthesized via a modified stöber method for capacitive deionization, *RSC Adv.* 6 (2016) 53542–53549, <https://doi.org/10.1039/c6ra06489b>.

[41] R. Wang, C. Xu, J. Sun, L. Gao, Three-dimensional Fe<sub>2</sub>O<sub>3</sub> nanocubes/nitrogen-doped graphene aerogels: nucleation mechanism and lithium storage properties, *Sci. Rep.* 4 (2014), 7171, <https://doi.org/10.1038/srep07171>.

[42] H. Fan, X. Huang, L. Shang, Y. Cao, Y. Zhao, L. Wu, C. Tung, Y. Yin, T. Zhang, Controllable synthesis of ultrathin transition-metal hydroxide nanosheets and their extended composite nanostructures for enhanced catalytic activity in the heck reaction, *Angew. Chem. Int. Ed.* 55 (2016) 2167, <https://doi.org/10.1002/anie.201508939>.

[43] L. Ding, D. Li, H. Shen, X. Qiao, H. Shen, W. Shi, 2D β-NiS as electron harvester anchors on 2D ZnIn<sub>2</sub>S<sub>4</sub> for boosting photocatalytic hydrogen production, *J. Alloy Compd.* 853 (2021), 157328, <https://doi.org/10.1016/j.jallcom.2020.157328>.

[44] A. Trenczek-Zajac, M. Synowiec, K. Zakrzewska, K. Zazakowny, K. Kowalski, A. Dziedzic, M. Radecka, Scavenger-supported photocatalytic evidence of an extended type I electronic structure of the TiO<sub>2</sub>@Fe<sub>2</sub>O<sub>3</sub> interface, *ACS Appl. Mater. Interfaces* 14 (2022) 38255–38269, <https://doi.org/10.1021/acsami.2c06404>.

[45] M. Xie, S. Duan, Y. Shen, K. Fang, Y. Wang, M. Lin, X. Guo, In-situ-grown Mg(OH)<sub>2</sub>-derived hybrid α-Ni(OH)<sub>2</sub> for highly stable supercapacitor, *ACS Energy Lett.* 1 (2016) 814–819, <https://doi.org/10.1021/acsenergylett.6b000258>.

[46] J. Li, L. Xiong, B. Luo, D. Jing, J. Cao, J. Tang, Hollow carbon sphere-modified graphitic carbon nitride for efficient photocatalytic H<sub>2</sub> production, *Chem. Eur. J.* 27 (2021) 16879–16888, <https://doi.org/10.1002/chem.202102330>.

[47] X. Zhang, P. Wang, X. Lv, X. Niu, X. Lin, S. Zhong, D. Wang, H. Lin, J. Chen, S. Bai, Stacking engineering of semiconductor heterojunctions on hollow carbon spheres for boosting photocatalytic CO<sub>2</sub> reduction, *ACS Catal.* 12 (2022) 2569–2580, <https://doi.org/10.1021/acscatal.1c05401>.

[48] J. Low, B. Dai, T. Tong, C. Jiang, J. Yu, In situ irradiated X-ray photoelectron spectroscopy investigation on a direct Z-scheme TiO<sub>2</sub>/CdS composite film photocatalyst, *Adv. Mater.* 31 (2019), 1802981, <https://doi.org/10.1002/adma.201802981>.

[49] T. Imrich, H. Krýsová, M. Neumann-Spallart, J. Krýsa, Fe<sub>2</sub>O<sub>3</sub> photoanodes: photocorrosion protection by thin SnO<sub>2</sub> and TiO<sub>2</sub> films, *J. Electroanal. Chem.* 892 (2021), 115282, <https://doi.org/10.1016/j.jelechem.2021.115282>.

[50] S. Wang, Y. Zhang, Y. Zheng, Y. Xu, G. Yang, S. Zhong, Y. Zhao, S. Bai, Plasmonic metal mediated charge transfer in stacked core-shell semiconductor heterojunction for significantly enhanced CO<sub>2</sub> photoreduction, *Small* 19 (2023), 2204774, <https://doi.org/10.1002/smll.202204774>.

[51] J. Liu, Y. Liu, N. Liu, Y. Han, X. Zhang, H. Huang, Y. Lifshitz, S. Lee, J. Zhong, Z. Kang, Metal-free efficient photocatalyst for stable visible water splitting via a two-electron pathway, *Science* 347 (2015) 970–974, <https://doi.org/10.1126/science.aaa3145>.

[52] Z. Li, W. Huang, J. Liu, K. Lv, Q. Li, Embedding CdS@Au into ultrathin Ti<sub>3-x</sub>C<sub>2</sub>Ty to build dual schottky barriers for photocatalytic H<sub>2</sub> production, *ACS Catal.* 11 (2021) 8510–8520, <https://doi.org/10.1021/acscatal.1c02018>.

[53] Y. Jiang, J. Liao, H. Chen, H. Zhang, J. Li, X. Wang, D. Kuang, All-solid-state Z-scheme α-Fe<sub>2</sub>O<sub>3</sub>/amine-RGO/CsPbBr<sub>3</sub> hybrids for visible-light-driven photocatalytic CO<sub>2</sub> reduction, *Chem* 6 (2020) 766–780, <https://doi.org/10.1016/j.chempr.2020.01.005>.

[54] Y. Xi, W. Mo, Z. Fan, L. Hu, W. Chen, Y. Zhang, P. Wang, S. Zhong, Y. Zhao, S. Bai, A mesh-like BiOBr/Bi<sub>2</sub>S<sub>3</sub> nanoarray heterojunction with hierarchical pores and oxygen vacancies for broadband CO<sub>2</sub> photoreduction, *J. Mater. Chem. A* 10 (2022) 20934–20945, <https://doi.org/10.1039/d2ta04278a>.

[55] Y. Zhang, H. Shi, S. Zhao, Z. Chen, Y. Zheng, G. Tu, S. Zhong, Y. Zhao, S. Bai, Hollow plasmonic p-metal-n S-scheme heterojunction photoreactor with spatially separated dual cocatalysts toward artificial photosynthesis, *Small* 20 (2024), 2304050, <https://doi.org/10.1002/smll.202304050>.

[56] Q. Chen, W. Mo, G. Yang, S. Zhong, H. Lin, J. Chen, S. Bai, Significantly enhanced photocatalytic CO<sub>2</sub> reduction by surface amorphization of cocatalysts, *Small* 17 (2021), 2102105, <https://doi.org/10.1002/smll.202102105>.

[57] S. Wang, Z. Li, G. Yang, Y. Xu, Y. Zheng, S. Zhong, Y. Zhao, S. Bai, Embedding nano-piezoelectrics into heterointerfaces of S-scheme heterojunctions for boosting photocatalysis and piezophotocatalysis, *Small* 19 (2023), 2102105, <https://doi.org/10.1002/smll.202302717>.

[58] J. Sheng, Y. He, J. Li, C. Yuan, H. Huang, S. Wang, Y. Sun, Z. Wang, F. Dong, Identification of halogen-associated active sites on bismuth-based perovskite quantum dots for efficient and selective CO<sub>2</sub>-to-CO photoreduction, *ACS Nano* 14 (2020) 13103–13114, <https://doi.org/10.1021/acsnano.0c04659>.

[59] W. He, Y. Wei, J. Xiong, Z. Tang, W. Song, J. Liu, Z. Zhao, Insight into reaction pathways of CO<sub>2</sub> photoreduction into CH<sub>4</sub> over hollow microsphere Bi<sub>2</sub>MoO<sub>6</sub>-supported Au catalysts, *Chem. Eng. J.* 433 (2022), 133540, <https://doi.org/10.1016/j.cej.2021.133540>.

[60] B. Lei, W. Cui, P. Chen, L. Chen, J. Li, F. Dong, C-doping induced oxygen-vacancy in WO<sub>3</sub> nanosheets for CO<sub>2</sub> activation and photoreduction, *ACS Catal.* 12 (2022) 9670–9678, <https://doi.org/10.1021/acscatal.2c02390>.

[61] P. Verma, A. Singh, F. Rahimi, P. Sarkar, S. Nath, S. Pati, T. Maji, Charge-transfer regulated visible light driven photocatalytic H<sub>2</sub> production and CO<sub>2</sub> reduction in tetraphiafulvalene based coordination polymer gel, *Nat. Commun.* 12 (2021) 7315, <https://doi.org/10.1038/s41467-021-27457-4>.